Article

Developmental Cell

Mechanosensation Dynamically Coordinates Polar Growth and Cell Wall Assembly to Promote Cell Survival

Graphical Abstract

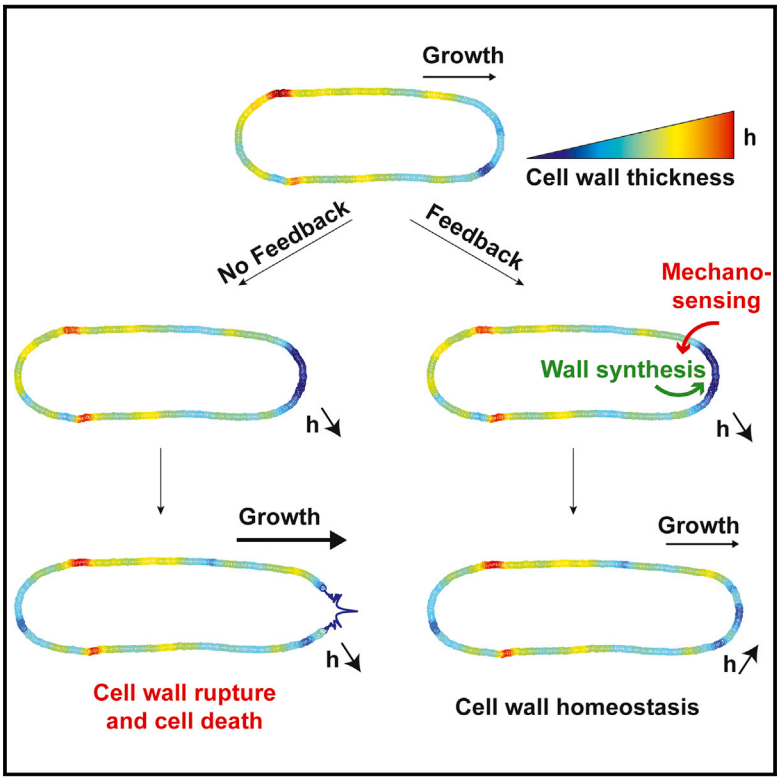

Highlights

- A new microscopy approach enables monitoring of cell wall (CW) thickness dynamics
- Cell wall mechanics are polarized, with growing domains being thinner and softer
- Cell growth and wall thickness negatively influence each other
- A feedback based on mechanosensing promotes cell wall homeostasis and cell survival

Authors

Valeria Davì, Hirokazu Tanimoto, Dmitry Ershov, ..., Etienne Couturier, Arezki Boudaoud, Nicolas Minc

Correspondence

arezki.boudaoud@ens-lyon.fr (A.B.), nicolas.minc@ijm.fr (N.M.)

In Brief

Davì et al. develop a sub-resolution microscopy method to monitor the dynamics of cell wall thickness and assembly in live fission yeast cells. They report thickness fluctuations with feedback, indicative of a mechanism for cell wall mechanical homeostasis important for cell integrity during normal growth.

Davì et al., 2018, Developmental Cell *45*, 170–182
April 23, 2018
https://doi.org/10.1016/j.devcel.2018.03.022

CellPress

CellPress

Developmental Cell
Article

Mechanosensation Dynamically Coordinates Polar Growth and Cell Wall Assembly to Promote Cell Survival

Valeria Davì,[1] Hirokazu Tanimoto,[1] Dmitry Ershov,[1] Armin Haupt,[1] Henry De Belly,[1,4] Rémi Le Borgne,[1] Etienne Couturier,[2] Arezki Boudaoud,[3,*] and Nicolas Minc[1,5,*]

[1]Institut Jacques Monod, CNRS UMR7592 and Université Paris Diderot, 15 rue Hélène Brion, 75205 Paris, France
[2]Laboratoire Matière et Systèmes Complexes, UMR7057, CNRS and Université Paris Diderot, 75205 Paris, France
[3]Reproduction et Développement des Plantes, Université de Lyon, ENS de Lyon, UCB Lyon I, INRA, CNRS, 46 Allée d'Italie, 69364 Lyon, France
[4]Present address: MRC-LMCB, University College London, WC1E 6BT London, UK
[5]Lead Contact
*Correspondence: arezki.boudaoud@ens-lyon.fr (A.B.), nicolas.minc@ijm.fr (N.M.)
https://doi.org/10.1016/j.devcel.2018.03.022

SUMMARY

How growing cells cope with size expansion while ensuring mechanical integrity is not known. In walled cells, such as those of microbes and plants, growth and viability are both supported by a thin and rigid encasing cell wall (CW). We deciphered the dynamic mechanisms controlling wall surface assembly during cell growth, using a sub-resolution microscopy approach to monitor CW thickness in live rod-shaped fission yeast cells. We found that polar cell growth yielded wall thinning and that thickness negatively influenced growth. Thickness at growing tips exhibited a fluctuating behavior with thickening phases followed by thinning phases, indicative of a delayed feedback promoting thickness homeostasis. This feedback was mediated by mechanosensing through the CW integrity pathway, which probes strain in the wall to adjust synthase localization and activity to surface growth. Mutants defective in thickness homeostasis lysed by rupturing the wall, demonstrating its pivotal role for walled cell survival.

INTRODUCTION

Growth control is of fundamental importance in biology, from the regulation of macromolecular assembly, cell physiology, up to organ development (Holley, 1975; Hong et al., 2016; Lander, 2011; Mahadevan and Mitchison, 2005). The growth of individual cells, for instance, has crucial implications for cell size determination, tissue homeostasis, or cancer progression (DeBerardinis et al., 2008a; Deberardinis et al., 2008b; Fantes and Nurse, 1977; Marshall et al., 2012; Thompson, 2010). To date, however, the mechanisms that control cellular growth remain poorly understood. This is because growth is an integrated output of multiple intertwined biochemical and biomechanical elements that dynamically probe and alter the cell surface to accommodate surface expansion. Those may include surface material synthesis mediated by processes such as exocytosis and endocytosis (Hepler et al., 2001; Novick and Schekman, 1979), as well as osmotic forces and mechanical elements that set the elasticity of the cell surface, such as the actin cortex, the glycocalyx, or the cell wall (CW) (Davi and Minc, 2015; Huang and Ingber, 1999; Salbreux et al., 2012). How those modules, which act at various time and length scales, may dynamically feed back onto each other to control the rate of cell surface expansion remains an outstanding open question.

Cell growth has been admittedly best documented in single walled cells, such as bacteria, fungi, or pollen tubes (Harris and Theriot, 2016; Mitchison and Nurse, 1985; Qin and Yang, 2011; Rojas et al., 2014). Those are among the fastest growing cells, with some fungal cells elongating at rates up to several tens of micrometers per minute (Lew, 2011; Qin and Yang, 2011). Size expansion in those cells is irreversible and limited by the synthesis of a thin and rigid sugar-made CW around the plasma membrane. The growth of the CW is thought to involve a complex balance between sugar synthesis, which builds the wall, and mechanical expansion driven by large internal turgor pressure, which puts the wall under tension to deform it (Cosgrove, 2005; Davi and Minc, 2015; Harold, 2002; McKenna et al., 2009). Because the CW bears large turgor-derived stress, it also provides mechanical integrity to those cells: removal or weakening of the CW yields near-immediate cell lysis and death. Given those considerations, cell growth may be seen as a dangerous process, as uncontrolled expansion and consequent thinning of the CW could compromise cell survival. To date, however, our understanding of how CW assembly and thickness may be dynamically controlled during cell growth has been limited, as historically it has been mostly studied with electron microscopy, which has biased our appreciation of the CW toward a static structure.

The biochemistry and genetics that support CW growth and composition have been well studied in model yeast cells (Lipke and Ovalle, 1998; Perez and Ribas, 2004). The rod-shaped fission yeast *Schizosaccharomyces pombe*, for instance, serves as a prime model for walled cell tip growth, stereotypical of many bacteria, fungi, and plant cells (Chang and Huang, 2014;

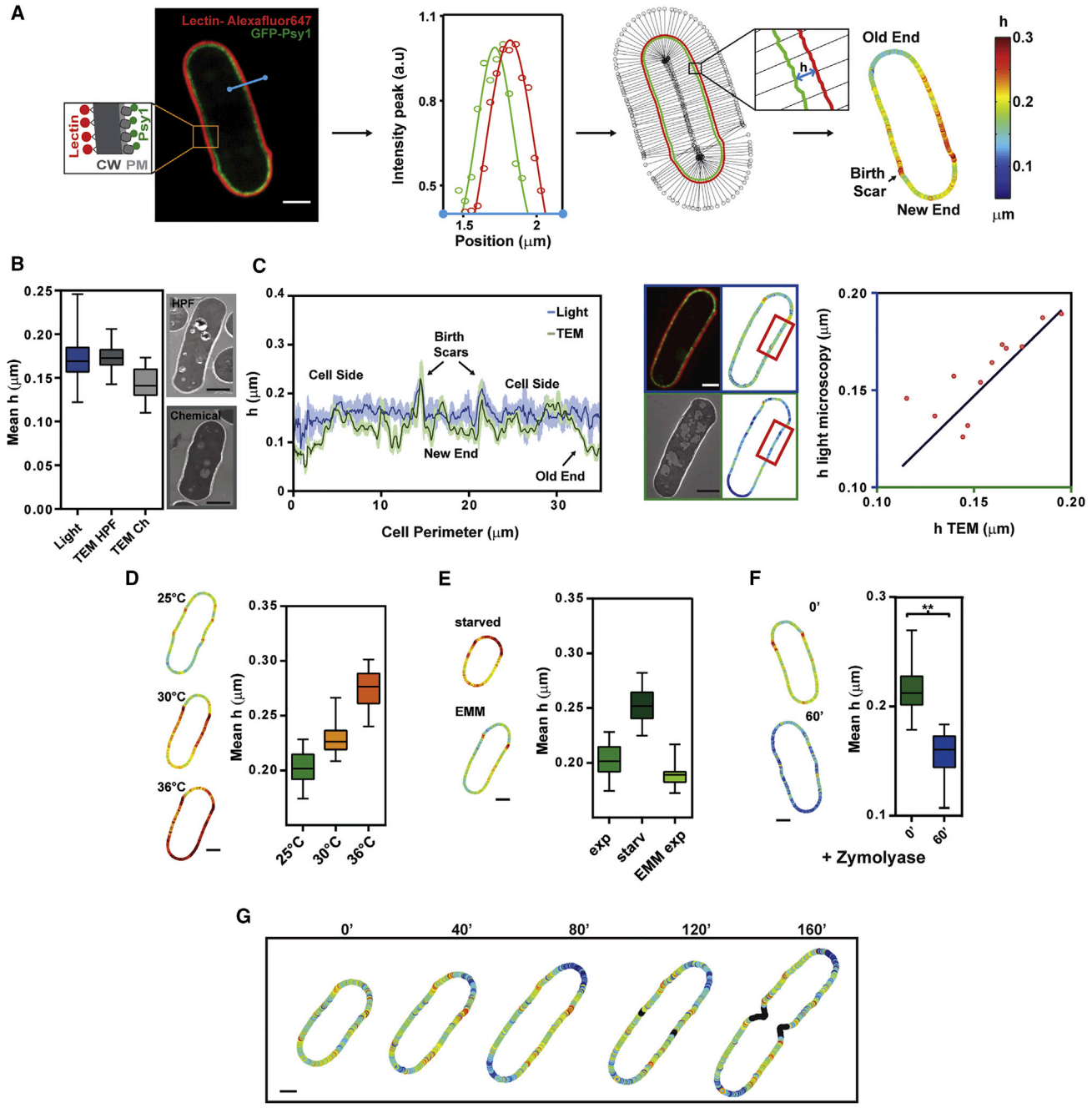

Figure 1. A Method to Image Cell Wall Thickness around Living Cells

(A) Mid-slice confocal image of a fission yeast cell expressing GFP-Psy1 (plasma membrane [PM]) and labeled with lectin-Alexafluor647 (CW outer surface). Contours are determined from the centers of Gaussian fits of each signal across the cell surface (blue line). After chromatic shift registration, the distance between the two contours yields local CW thickness measurements (h). (Right) Thickness color map around a cell.

(B) Measurement of CW thickness using photonic microscopy (n = 41) and TEM performed by high-pressure freezing (HPF) (*n=23*) or chemical fixation (Ch) (*n=22*). Representative TEM images in these conditions.

(C) (Left) Running average (on 10 pixels) and SD of thickness measurement of the same single cell, shown in the middle, measured by TEM or light microscopy using CLEM. (Right) Light versus TEM thickness measurement averaged over regions of ~2 μm (red rectangle) (n = 13 regions, from nine cells). The line is a linear fit. Light microscopy measurements for CLEM are corrected to compensate for the high internal fluorescent background caused by chemical fixation (see STAR Methods).

(D) Mean wall thickness of cells grown at different temperatures, and representative thickness color maps in the same conditions (n > 25 for each condition).

(E) Mean wall thickness of cells measured in exponential phase (exp) or after ~16 hr of starvation (starv), and in cells grown in Edinburgh minimal medium (EMM) (n > 25 for each condition).

(legend continued on next page)

Chang and Martin, 2009; Davi and Minc, 2015). The fission yeast CW behaves as a thin elastic shell with an elastic modulus estimated to be around 30–50 MPa, which resists an internal turgor pressure of 1–1.5 MPa (Abenza et al., 2015; Atilgan et al., 2015; Minc et al., 2009). In those cells, CW synthesis is first restricted to the old cell tip after division, and is redistributed to both growing tips after NETO (New End Take Off), and to the cell middle for septation (Cortes et al., 2005). At cell tips, wall synthesis is catalyzed by one α-glucan (Ags1) and three β-glucan (Bgs1, Bgs3, and Bgs4) synthases, which elongate glucan fibers, as well as glucanosyl-transferases enzymes (Gas1 and Gas2) and one putative exo-glucanase, Exg2, which may remodel and/or crosslink glucan fibers at cell tips (Davi and Minc, 2015; Perez and Ribas, 2004). Those enzymes are under the control of the activity of the highly conserved Rho-GTPases, Rho1 and Rho2, which are activated by the GEFs Rgf1 and Rgf2 (Arellano et al., 1999; Garcia et al., 2006). Damage to the CW, such as that caused by antifungal agents, is monitored by the CW integrity (CWI) pathway, which may be activated by Rgf1, Rho1, or Rho2, and triggers the expression of a set of CW repair genes through the Pmk1 MAPK (Garcia et al., 2009b; Perez and Cansado, 2010).

To understand how those different biochemical layers dynamically influence and probe the mechanics of the CW, we here introduce a microscopy method to directly measure CW thickness all around live growing fission yeast cells. We find that CW thickness at growing cell tips is highly dynamic in time, with phases of thickening followed by thinning phases, and vice versa. We demonstrate a homeostatic system that accounts for thickness fluctuations and stable values at the cell population. Homeostasis is supported by mechanosensing activities of the CWI that probe cellular growth as a mechanical stress and dynamically adjust synthesis to growth rates. Mutants defective in homeostatic thickness lyse by over-thinning the CW. This work provides evidence for mechanochemical feedbacks promoting growth control and cell survival.

RESULTS

A Sub-resolution Method to Monitor CW Thickness Dynamics in Living Cells

The fission yeast CW is a thin layer of typically 100–200 nm, below the resolution of light microscopy. Given large internal turgor pressure, the plasma membrane is plastered against the internal face of the CW (Osumi, 2012). In addition, glycosylated galactomannan proteins are secreted in the CW and can be selectively detected on the most outer surface of the wall with specific lectins (Horiseberger and Rosset, 1977). We exploited those properties to develop a sub-resolution method to compute CW thickness all around single live growing fission yeast cells. We labeled the inner and outer faces of the CW respectively using an integral membrane SNARE protein tagged with a GFP at its intracellular tail (GFP-psy1) (Nakamura et al., 2001) and by adding lectins from *Griffonia simplicifolia* that specifically bind the most outer face of the fission yeast CW, labeled with a different emitting fluorophore. Following image registration and cell contour segmentation, we computed the distance between the centers of the two fluorescent signals along lines bisecting the cell surface, which provided a local measurement of CW thickness (Chugh et al., 2017; Clark et al., 2013). Thickness measured by those means could be calculated with a precision around ~30 nm and a lateral resolution of ~500 nm, and was represented as colored cellular maps (Figures 1A and S1A–S1E) (see STAR Methods). Measurements were slightly sensitive to growth environment and media but robust to variations in lectin-bound fluorophores or membrane associated GFP signals (Figures S2A–S2C).

To validate our approach, we first compared it with transmission electron microscopy (TEM) measurements, which serve as the current standard to image the CW (Osumi, 2012). The mean CW thickness in a wild-type (WT) population measured by our method was 170 ± 23 nm. This was comparable with values obtained from high-pressure freezing TEM (172 ± 14 nm) and ~16% higher than values obtained in chemical fixation TEM (143 ± 19 nm), plausibly because chemical fixation may not fully protect the CW against subsequent resin embedding (Osumi, 2012) (Figure 1B). Next, we used correlative light electron microscopy (CLEM) to image and compute CW thickness in the same cell with TEM and our method. Although the use of high-pressure freezing did not allow the retention of fluorophores needed for CLEM, we could directly compare thickness values in individual chemically fixed cells. This CLEM analysis yielded nearly similar patterns of thickness along the cell boundary, supporting the reliability of our method as a local measurement of CW thickness (Figures 1C and S2D–S2G).

To assess the accuracy, precision, and range of this live imaging method, we next tested it against conditions thought to affect CW thickness. As previously suggested, we detected a dose-dependent increase in CW thickness with temperature or as a result of prolonged starvation (Figures 1D and 1E) (Cassone et al., 1979). Cells treated with zymolyase, a CW digesting enzyme, exhibited significant CW thinning (Figure 1F). Finally, thickness could be imaged in the same cell over several hours with no major cellular damage and no impact of bleaching on the measurement (Figures 1G, S3A, and S3B and Videos S1 and S2). Thus, it was possible to quantify the dynamics of CW thickness and assembly with unprecedented accuracy in populations of live growing cells.

Polar Growth Sites Are Associated with Thinner and Softer CWs

Given that wall assembly in fission yeast is restricted to growing cell tips during interphase and to the cell middle during septation, we computed CW thickness patterns in cell populations (Chang and Martin, 2009; Davi and Minc, 2015). Birth scars that are inherited from previous cell division were associated with a significantly thicker CW, with a thickness of h_{scar} = 224 ± 20nm. Interestingly, we observed that the CW was consistently thinner at the old end, the end that grows most during

(F) Thickness before (n = 35 cells) or after 60′ of zymolyase treatment (n = 19); **p < 0.0001.
(G) Time lapse of CW thickness maps of a growing cell. Black points correspond to positions in which thickness cannot be measured accurately. Scale bars, 2 μm; whisker plots show the median and full dataset range.
See also Figures S1–S3 and Videos S1 and S2.

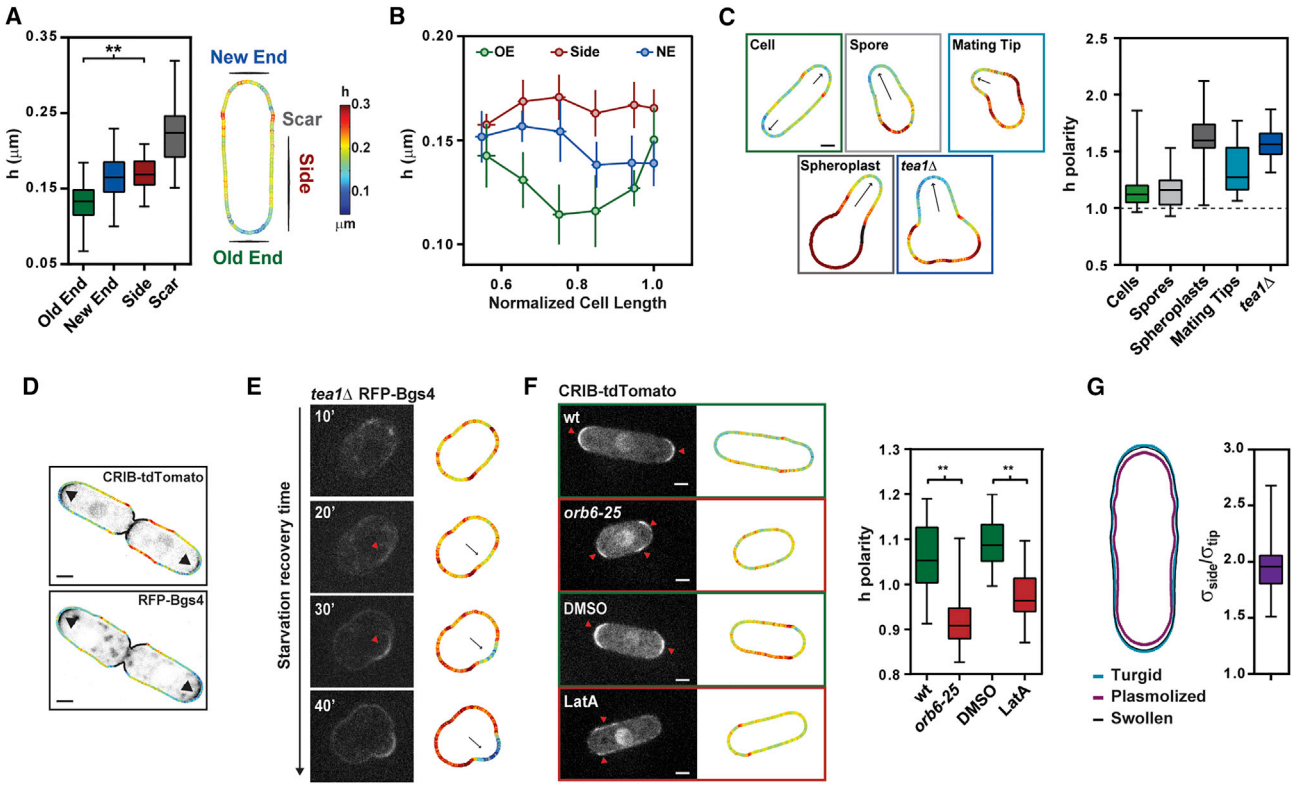

Figure 2. Cell Polarity and Cell Wall Thickness Patterns

(A) Thickness color map of a typical interphase cell, and thickness values at the old end (n = 50), new end (n = 41), cell sides (n = 51), and birth scars (n = 47).

(B) Evolution of cell wall thickness as a function of cell length (used as a proxy for cell cycle progression), in WT cells at the old end (OE; n = 12 cells), the new end (NE; n = 8 cells), and cell sides (n = 12 cells). Cell length is normalized by the length at septation.

(C) Representative thickness color maps and thickness polarity in WT interphase cells (n = 41), outgrowing spores (n = 24), recovering spheroplasts (n = 22), mating tips (n = 18), and *tea1Δ* cells recovering from starvation (n = 29). Arrows indicate growth directions. h polarity is defined as the side/tip ratio in WT interphase cells using an average of both tips values, and back/tip ratio in the other cases.

(D) Superimposition of h map and polar growth markers (arrowheads).

(E) Mid-slice confocal time-lapse and h maps of a *tea1Δ* cell recovering from starvation. Arrows indicate growth direction and arrowheads point at RFP-Bgs4 polar cap.

(F) (Left) Mid-slice confocal image and h maps in the indicated conditions. Red arrowheads point at CRIB-td-Tomato polar caps. (Right) h polarity in WT (*n=30*) and *orb6-25* (*n=29*) grown for 2 hr at restrictive temperature and in cells treated for 30′ with DMSO (*n=21*) or 100 μM LatA (*n=26*).

(G) (Left) Symmetrized cell boundary in turgid, plasmolyzed, and computationally swollen state, used to compute local elastic moduli, Y, at cell tips and sides. (Right) Ratio of surface modulus, σ = hY, between tips and sides (n = 21 cells). Scale bars, 2 μm; whiskers plots show median and full dataset range. Error bars represent SD. **p < 0.0001. Black points in thickness maps correspond to positions in which thickness cannot be measured accurately.

See also Figure S3 and Video S3.

interphase, h_{oe} = 130 ± 26 nm, compared with cell sides, h_{side} = 170 ± 20 nm. Thickness at the new end, which only initiates growth after NETO was in contrast only slightly thinner than cell sides, with a mean value of h_{ne} = 167 ± 14 nm (Figure 2A). To quantify how those values may evolve during the cell cycle, we performed long time lapses following full ~3 hr cell cycles in populations of cells, with a temporal resolution of 20'. In a WT population, this revealed a global decrease of thickness at the old end in the first part of the cell cycle, followed by a steady increase in the following phase, eventually yielding similar values to the beginning of the cycle. Tip thinning was also observed at the new end but delayed by the time needed for the new end to start growing at NETO. Thickness at cell sides exhibited much less variations than at cell tips (Figure 2B).

We also found that monopolar tips of outgrowing spores, spheroplasts, mating projections, and of *tea1Δ* mutants branching from cell sides were also markedly thinner at the front growing site than on the non-growing back (Bonazzi et al., 2014; Kelly and Nurse, 2011; Mata and Nurse, 1997; Petersen et al., 1998) (Figure 2C). These thin wall regions at sites of polar growth co-localized with the downstream polarity regulator GTP-Cdc42 (visualized with a CRIB domain fused to td-Tomato) and with the β-glucan synthase Bgs4, which mark sites of CW assembly and remodeling (Cortes et al., 2005; Tatebe et al., 2008) (Figure 2D). Furthermore, time lapse of polarized regrowth in *tea1Δ* cells recovering from starvation showed the stabilization of a Bgs4 polar domain, concomitant with local CW thinning and followed by the emergence of a new growing tip (Figure 2E and Video S3). Importantly, full depolymerization of actin with 100 μM Latrunculin A or the use of an *orb6-25* thermo-sensitive allele affecting Cdc42-based polarity both yielded the detachment of GTP-Cdc42 polar domains from cell tips and

consequent alteration of CW thickness patterns within tens of minutes (Bendezu and Martin, 2011; Das et al., 2009) (Figure 2F).

The CW was also softer at growing cell tips. This was shown by computing CW elastic moduli, Y, which characterizes the bulk mechanical properties of the CW. To this aim, we plasmolyzed cells by rapidly adding 1.5 M sorbitol to the medium in microfluidic flow channels, which causes a rapid drop in turgor pressure, and consequent cell shrinkage (Abenza et al., 2015; Atilgan et al., 2015; Bonazzi et al., 2014). Using the changes in cell shapes between inflated and plasmolyzed states and local thickness values, we could extract values of CW elastic moduli at cell tips and at cell sides, to be Y_{tip} = 45.3 ± 0.7 MPa, and Y_{side} = 72.5 ± 1.15 MPa, yielding a ratio in surface moduli ($\sigma = hY$) of $\sigma_{side}/\sigma_{tip}$ = 1.96 ± 0.27 (Figures 2G, S3C, and S3D). Together, those results suggest that internal polarity, which directs growth and CW synthesis, causes sites of polar growth to have thinner and softer CWs.

Contribution of Synthesis and Growth to CW Thickness at Cell Tips

Those findings prompted us to assess how CW thickness and assembly may be regulated at sites of polar growth. We first considered a minimal theoretical model for thickness dynamics at cell tips (Figure 3A). We posited that the CW thickens through synthesis and thins through cell elongation, which, given mass conservation, yields a dynamic evolution of h_{tip}:

$$\frac{dh_{tip}}{dt} = S - \gamma\, h_{tip}, \qquad \text{(Equation 1)}$$

where S is a rate of wall synthesis per unit surface and γ the strain rate of the CW. Accordingly, CW thickness is determined by the balance between synthesis and wall expansion, which explains the observation that thickness may not be directly positively correlated with Bgs4 signal (Figure 2D). The strain rate γ is related to the cell elongation rate, Gr, by the curvature radius at the tip, R_c:

$$Gr = dL/dt = qR_c\,\gamma, \qquad \text{(Equation 2)}$$

with L the length of the cell and q a numerical geometrical prefactor.

To assay the contribution of synthesis, we performed experiments to manipulate synthase activity. In cells overexpressing Pck2, a positive regulator of glucan synthesis, one major component of the fission yeast CW, we could detect significant thickening, up to ~900 nm in some cells (Arellano et al., 1999). Thickening was also observed by overexpressing a constitutively active Rho1 allele, *rho1-G15V* (Arellano et al., 1996) (Figure 3B). Conversely, a *cwg1-1* thermo-sensitive allele of the glucan synthase Bgs4 exhibited significant thinning at growing cell tips, consistent with previous TEM observations (Muñoz et al., 2013) (Figure 3C). As a more direct assay, we also reduced CW synthesis with low doses of caspofungin, a drug that specifically impairs β-glucan synthase activity (Martins et al., 2011). This treatment led to a net thickness decrease at growing ends over tens of minutes, eventually causing aberrant cell bulging at longer times (Figure 3D and Video S4).

Using those caspofungin treated cells, in which synthesis is partially impaired, we also computed the contribution of growth to thickness variation. We measured the relative changes in thickness, $\Delta h_{oe}/h_{oe}$, which, given Equations 1 and 2, is predicted to linearly scale with $-\Delta L_{oe}/R_c$. This analysis yielded a negative linear correlation with a slope of −0.81 (correlation coefficient, r = −0.57), and a positive y-intersect, which could correspond to remaining CW α-glucan synthesis in the presence of this drug (Figure 3E). Together, those data support a simple model for CW thickness evolution positively regulated by synthesis and negatively by growth.

Influence of CW Thickness on Cell Growth Rates

As the balance between turgor and CW mechanics has been proposed to set growth rates in fission yeast (Bonazzi et al., 2014; Minc et al., 2009), we sought to investigate the influence of thickness on strain and growth rates. Using a simple model for wall rheology (Minc et al., 2009; Rojas et al., 2011), we posited that the strain rate could be written as:

$$\gamma = r\frac{PR_c}{Yh_{tip}}, \qquad \text{(Equation 3)}$$

with r a wall remodeling rate, Y the elastic modulus of the wall, and P the turgor pressure (we here neglect a possible threshold in turgor for growth to occur). Given Equation 2, this assumption implies that the elongation rate Gr scales with R_c^2/h_{tip}. This scaling was confirmed using three-dimensional numerical simulations of a mechanical model of fission yeast growth (Abenza et al., 2015) (Figure 3F).

Experimentally, we first tested this model prediction by comparing the mean growth rate and thickness at the population level at different moments in the cell cycle. This showed that growth rates were indeed anti-correlated with thickness values (Figure S4A). We then used time-lapse videos to compute and plot single cell elongation rates, as a function of initial tip curvature radii and CW thickness. To vary R_c, we used WT cells and mutants with larger (*rga4Δ*) and smaller diameters (*rga2Δ*), as well as microfabricated channels to physically diminish the diameter of *rga4Δ* cells (Das et al., 2007; Villar-Tajadura et al., 2008; Zegman et al., 2015). This analysis yielded, as predicted, a robust linear dependency between Gr and R_c^2/h_{tip}, indicating that CW thickness could serve as a major determinant influencing elongation rates (Figures 3G–3I).

Homeostasis in CW Thickness through Strain Mechanosensing

The above findings suggest that, without regulatory layers, growth and thickness may negatively regulate each other, which could potentially lead to catastrophic situations of cell lysis through CW thinning or growth arrest through thickening. We thus computed tip thickness evolution in single cells over several hours, with a high temporal resolution of 6 min, focusing on the old end. Strikingly, this revealed a thickness fluctuating behavior with feedback, consisting of multiple phases of CW thickening, followed by thinning phases, and so on. Thickness on cell sides was, in contrast, almost completely stable (Figures 4A, 4B, and S4B–S4E). Fourier spectrum analyses allowed to clearly discern those fluctuations from the global trend at the cell cycle level, and yielded an estimate of the timescale for the feedback around 50–60 min (Figures S4F and S4G). Those

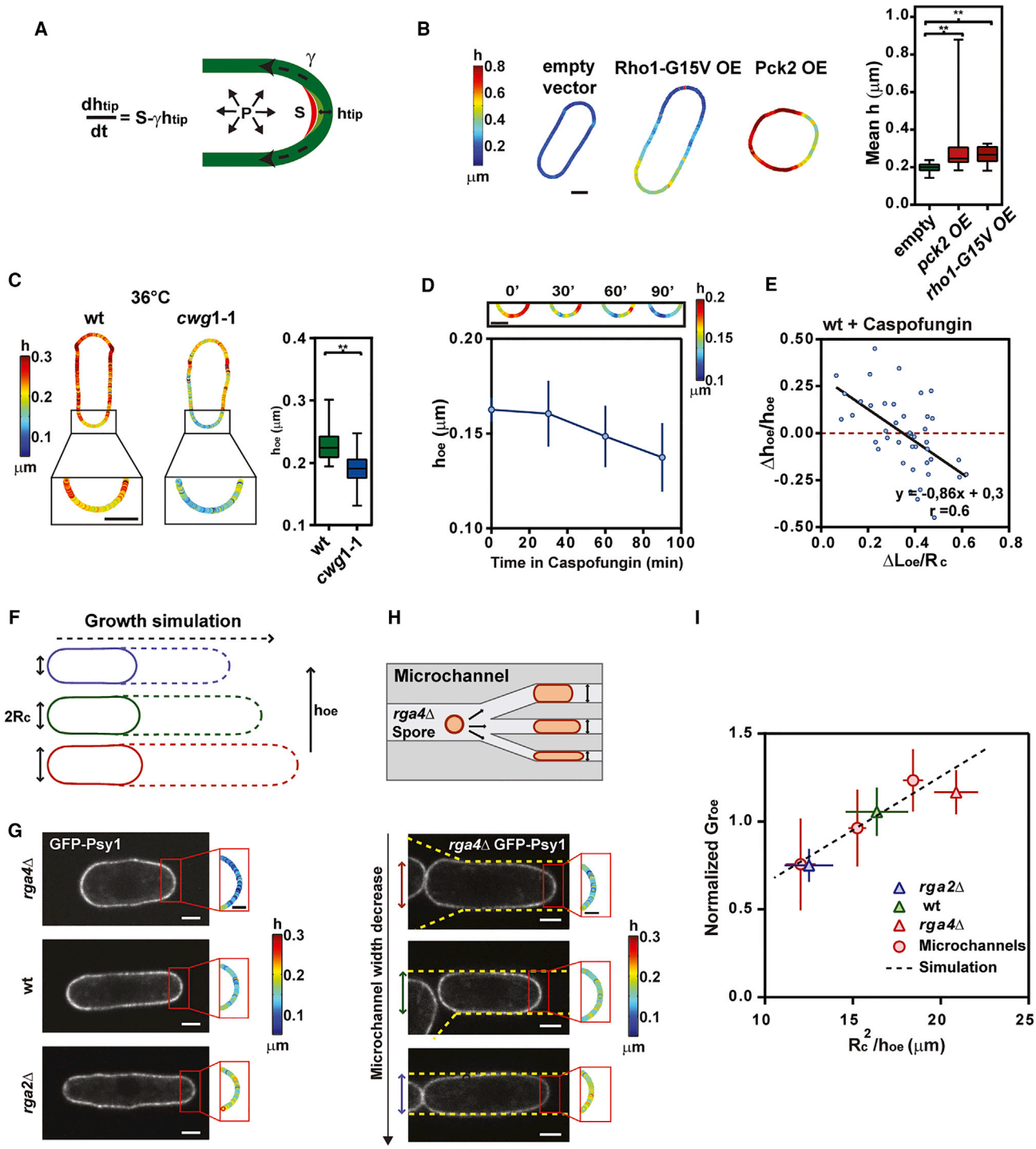

Figure 3. Dynamics of Cell Wall Assembly at Polar Growth Sites

(A) Simple model for tip thickness (h_{tip}) dynamics. S is a rate of wall synthesis per unit surface, γ the strain rate, and P the turgor pressure.

(B) Representative color maps and mean h measurement of cells overexpressing a control empty plasmid (n = 59 cells), a constitutively active Rho1-G15V allele (n = 27), and Pck2 (n = 59).

(C) Representative color maps and thickness values at the old end (h_{oe}) in WT (n = 27) and *cwg1-1* (n = 29) grown at restrictive temperature.

(D) (Top) Representative h_{oe} maps following caspofungin treatment, and evolution of h_{oe} in time (bottom, n = 11 cells).

(E) $\Delta h_{oe}/h_{oe}$, measured in caspofungin treated WT cells and plotted as a function of $\Delta L_{oe}/R_c$ (n = 12 cells). The black line is a linear fit.

(F) Growth simulations: plain and dashed lines mark cell shapes at the beginning and the end of the simulation.

(G) Mid-slice confocal images of typical *rga4Δ*, WT, and *rga2Δ* cells expressing the membrane marker GFP-Psy1 and close-up local h color maps at the old end.

(legend continued on next page)

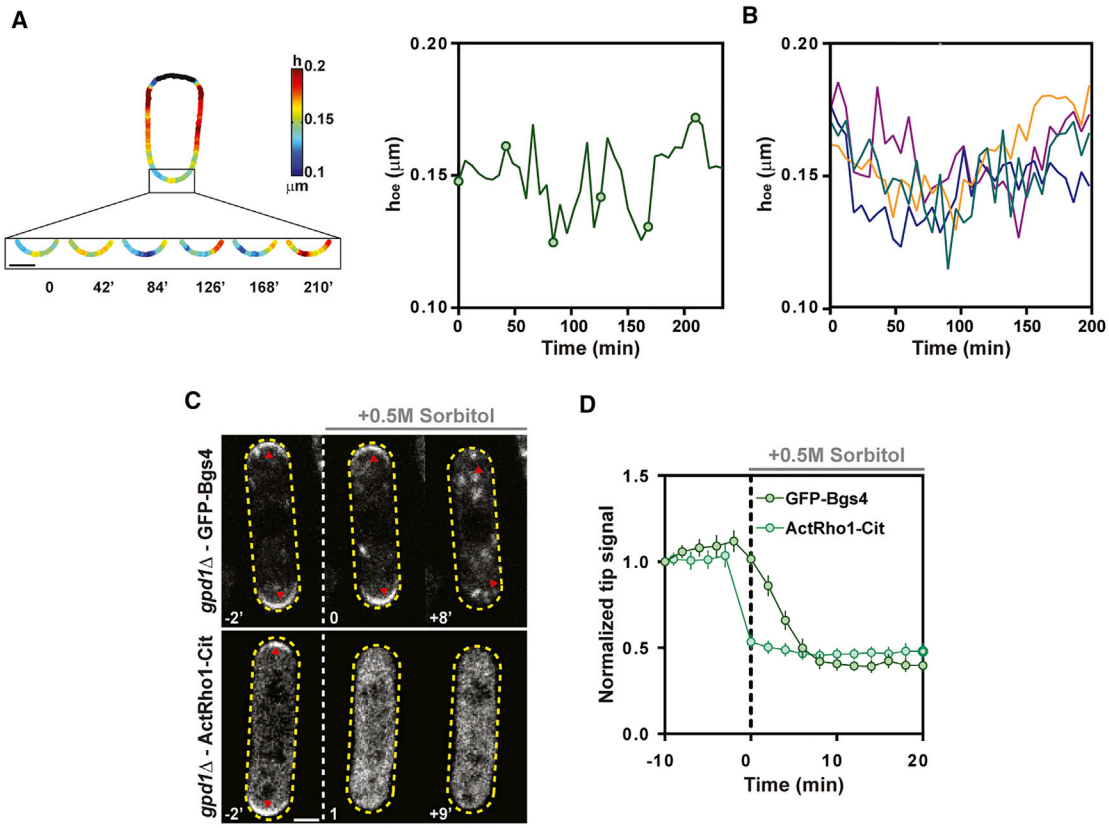

Figure 4. Cell Wall Thickness Fluctuations and Strain Rate-Dependent Cell Wall Synthase Activation and Localization

(A) Close-up views on thickness maps (smoothed on 10 pixels) at the old end of a growing WT cell, and corresponding plots of thickness evolution at the old end within a full cell cycle. Black points correspond to positions in which thickness cannot be measured accurately. Dots correspond to time points shown in color plots.

(B) Evolution of thickness at the old end h_{oe} imaged at 6 min interval for one cell cycle in four representative WT cells.

(C) GFP-Bgs4 and Active-Rho1-Citrin polar domains (arrowheads) detachment in *gpd1Δ* cells following turgor reduction caused by the addition of 0.5 M sorbitol in the medium.

(D) Evolution of normalized tip signal of GFP-Bgs4 (n = 14) and Active-Rho1-Citrine (n = 18) in cells rinsed with sorbitol at t = 0. Scale bars, 2 µm; error bars represent SD. Scale bars, 2 µm.

See also Figure S5.

fluctuations at cell tips suggested the presence of a delayed feedback dynamically regulating CW thickness and assembly at growing tips.

Based on reported observations in fission yeast and other cell types (Bonazzi et al., 2014; Nakayama et al., 2012), we assayed a potential positive feedback between growth, or equivalently strain rate, and polarized synthesis. To reduce strain rate, we rapidly decreased turgor by rinsing cells with medium containing 0.5 M sorbitol using a *gpd1Δ* background to prevent turgor adaptation (Minc et al., 2009). This caused an immediate growth arrest and the rapid detachment of active-Rho1 polar domains (Davidson et al., 2015) followed by the detachment of Bgs4 domains over the subsequent minutes (Figures 4C, 4D, and S4H). Those data suggest that CW synthase activity and localization may be actively sensitive to growth or strain rates.

To incorporate mechanical sensing in our model, we used a general delayed dependence, between strain rate and synthesis, of the form: $S(t) = S_0 + \lambda\gamma(t-T)$, with S_0 a basal synthesis rate, λ a positive parameter characterizing the strength of the sensing, and T a delay in the response between strain and synthesis, so that:

$$\frac{dh_{tip}}{dt}(t) = \left(S_0 - \frac{rPR_C}{Y}\right) + \lambda\frac{rPR_C}{Y}\frac{1}{h_{tip}(t-T)}. \quad \text{(Equation 4)}$$

Using the evolution of old end thickness in single cells, we thus evaluated experimentally the dependence of the thickness rate,

(H) Schematic for diameter manipulation in microchannels, and mid-slice confocal images of *rga4Δ* cells grown in microchannels with different diameters and close-up local h color maps at the old end. The yellow dashed lines mark the border of the microchannels.

(I) Normalized growth rate at the old end plotted as a function of R_c^2/h_{oe}, for WT (n = 36), *rga2Δ* (n = 26), *rga4Δ* (n = 37), and *rga4Δ* cells grown in microchannels (n = 33, binned on 11, 10, 13 cells). The dotted line is a fit of the growth simulation results. Whiskers plots show median and full dataset range. r is a Pearson correlation coefficient. Error bars correspond to SD. **p < 0.0001. Scale bars represent 2 µm in confocal images and full cell color maps, and 1 µm in insets.

See also Figure S4 and Video S4.

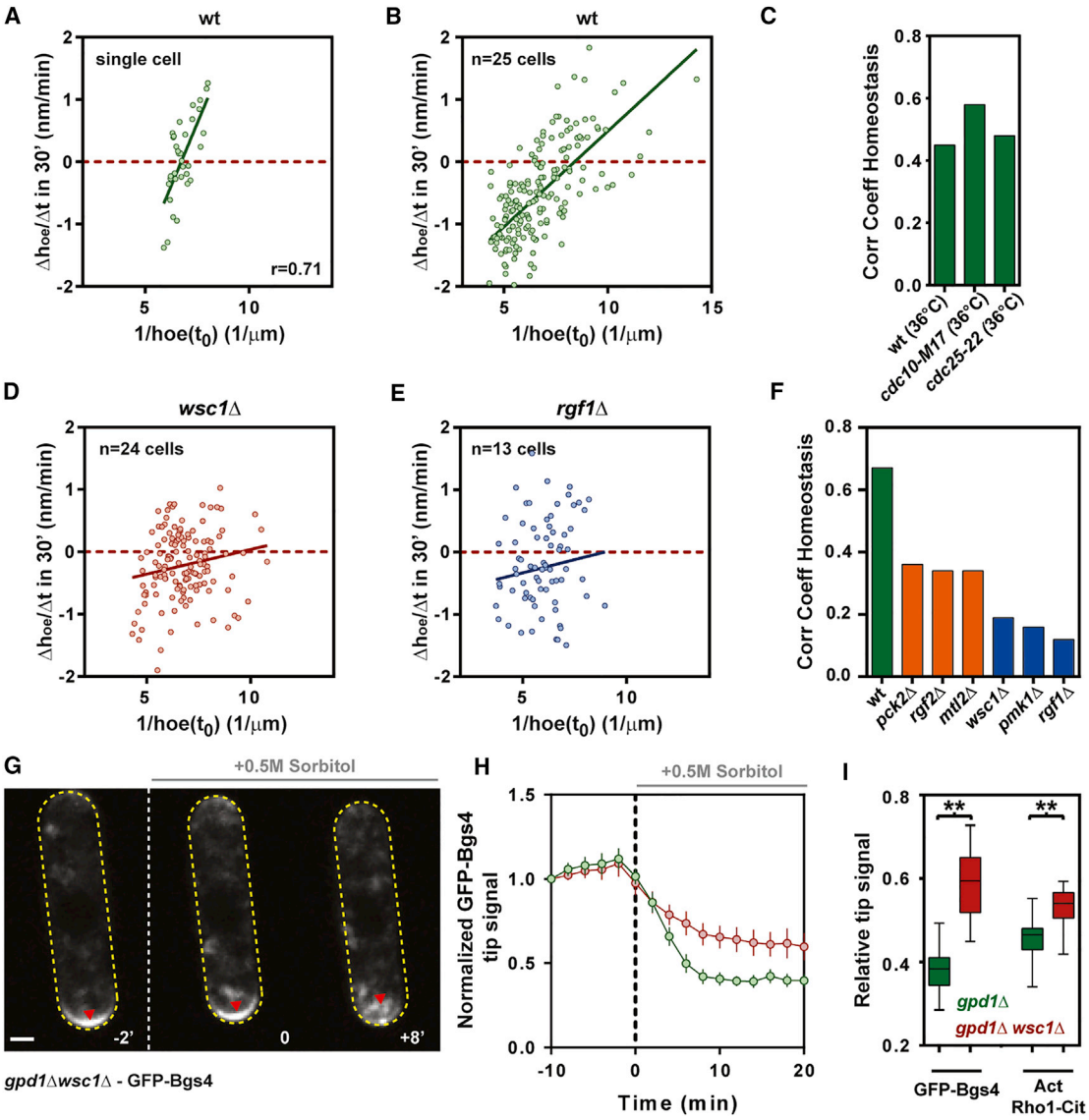

Figure 5. The Cell Wall Integrity Pathway Mediates Cell Wall Thickness Homeostasis

(A and B) (A) Thickness homeostasis plot in a single WT cell imaged during a full cell cycle at 6′ interval. $\Delta h_{oe}/\Delta t$ is computed as $(h_{oe}(t_0+30')-h_{oe}(t_0))/30$, for various t_0 and plotted as a function of $1/h_{oe}(t_0)$ (B) Thickness homeostasis plot in a population of WT cells (n = 25 time lapses of individual cells). The plain line is a linear fit.

(C) Pearson correlation coefficient of thickness homeostasis for WT (35 cells), *cdc10-M17* (13 cells), and *cdc25-22* (19 cells) grown at restrictive temperature (36°C).

(D and E) (D) Thickness homeostasis plot for a *wsc1Δ* mutant (24 cells). (E) Thickness homeostasis plot for a *rgf1Δ* mutant (13 cells). Plain lines are linear fits.

(F) Pearson correlation coefficient for thickness homeostasis of WT (25 cells), *mtl2Δ* (24 cells), *pck2Δ* (27 cells), *rgf2Δ* (22 cells), *wsc1Δ* (24 cells), *rgf1Δ* (13 cells), and *pmk1Δ* (25 cells).

(G) Defect in GFP-Bgs4 detachment in response to turgor reduction in a *gpd1Δwsc1Δ* double mutant. Note the remaining signal compared with a *gpd1Δ* single mutant shown in Figure 4C. Arrowheads point to a GFP-bgs4 polar domain.

(H) Evolution of normalized tip signal of GFP-Bgs4 (n = 19) in *gpd1Δ* and *gpd1Δwsc1Δ* cells rinsed with sorbitol at t = 0.

(I) Ratio between tip signals of the indicated markers after and before sorbitol treatment in *gpd1Δ* and *gpd1Δwsc1Δ* cells (n = 14, 19, 18, 18). The excess of negative points in homeostasis plots is caused by an oversampling in the first part of the cell cycle. r is the Pearson correlation coefficient. Whiskers plots show median and full dataset range. Error bars represent SD. **p < 0.0001. Scale bars, 2 μm.

See also Figures S5 and S6.

$dh_{oe}/dt(t_0 + T)$, computed at different delays, on the inverse of initial thickness $1/h_{oe}(t_0)$, measured at various t_0 in time lapses. We found a positive correlation at delays starting around 12 min (r = 0.4), which improved for longer delays, yielding highest correlations at delays around 30–40 min (r = 0.7), in agreement with Fourier spectrum analyses (Figures 5A, 5B, and S5A–S5E). In this plot, the x-intercept corresponded to a homeostatic thickness of $h_{oe}^* = 119$ nm, close to the mean thickness of the old end at the population level. Importantly, this homeostatic behavior was not influenced by cell cycle driven thickness variations and was still

observed in *Cdc10-M17* and *Cdc25-22* mutants respectively blocked in G1 or in G2 phase, ruling out putative contribution of cell cycle variations to this behavior (Figures 5C and S5F–S5I). Solving the delayed differential Equation 4 for h(t) yielded, in a range of parameter values, fluctuating behavior, reminiscent of experimental observations (Figures S5J–S5L and Supplemental Information). Together those findings support the existence of a homeostatic mechanism, in which an overshoot (or an undershoot) in thickness is corrected by thinning (respectively thickening) the wall over the subsequent tens of minutes to maintain it around a narrow range of values.

The CWI Pathway Mediates Strain Mechanosensing for Thickness Homeostasis

A prime candidate system that may sense CW properties and influence synthesis is the CWI, a signaling cascade involved in general CW stress response (Perez and Cansado, 2010). In fission yeast, this pathway is thought to be activated at the cell surface by the putative trans-membrane stress sensors Wsc1 and Mtl2, which interact with the CW, plausibly through long serine/threonine rich domains extending in the CW matrix (Cruz et al., 2013). Those factors signal downstream to Rho-GEFs Rgf1 and Rgf2, which may directly regulate the Rho-GTPases Rho1 and Rho2 for glucan synthase activation (Garcia et al., 2006, 2009a; Mutoh et al., 2005). The CWI also triggers the activation of gene transcription for CW repair, through the Pmk1 MAPK cascade (Garcia et al., 2009b; Perez and Cansado, 2010). By performing a candidate screen on single mutants of the CWI, we found that *wsc1Δ*, *rgf1Δ*, and *pmk1Δ* were severely defective in thickness homeostasis, with changes in thickness being mostly independent on previous thickness values (Figures 5D–5F, S6A, and S6B). Importantly, those mutants still exhibited global thinning and thickening phases during the cell cycle, suggesting those large-scale variations are independent of the CWI (Figure S6C). In addition, we found that the detachment of Bgs4 and active-Rho1 polar domains as a response to pressure and strain reduction in a *gpd1Δ wsc1Δ* mutant was significantly less pronounced than in a *gpd1Δ* alone, suggesting that Wsc1 may directly probe CW strain rate to tune synthesis through the CWI (Figures 5G–5I and S6D).

Finally, we assayed whether the implication of the CWI pathway in thickness homeostasis could account for the lysis phenotype of some CWI mutants during normal growth (Cruz et al., 2013; Garcia et al., 2006). By imaging thickness evolution in *rgf1Δ*, we observed in ~30% of cases cells that started with a relatively thick wall and little growth, which switched incidentally to a phase of unusually rapid growth concomitant with rapid CW thinning eventually causing tip lysis and cell death (Figures 6A and 6B). We noted, however, that the thickness at which lysis occurred in some of those cells could have values similar to WT tips. As the failure strain of the CW yielding to lysis may depend on the surface modulus, $\sigma = Yh$, which has contributions from both thickness and elastic modulus, we suspect that those cells also have lower bulk modulus, arising from misregulated CW composition. This was supported by the similar growth rate values that individual *rgf1Δ* cells reached before lysis, which is predicted to inversely depend on the surface modulus (Figure 6B). Similar lysis phenotype was also observed in *wsc1Δ*, but to a much lesser extent, which precluded a careful analysis of thickness dynamics. Together those findings demonstrate that the CWI may directly probe CW strain rates to adjust synthesis, thereby coordinating growth and CW assembly needed for cell survival (Figure 6C).

DISCUSSION

The mechanical properties of the CW and turgor values underlie walled cells' growth and shapes, and have been redundantly used as tunable cellular properties to survive, colonize, infect, or reproduce (Bastmeyer et al., 2002; Dagdas et al., 2012; Dudin et al., 2015; Harold, 2002; Keegstra, 2010; Lew, 2011; Silhavy et al., 2010). This importance contrasts with the limited knowledge we have on the dynamic regulation of those mechanical parameters in growing and dividing cells. By developing and validating here the very first approach to monitor CW thickness in live cells, we provide evidence of key contributions of the polarized dynamics of the CW for growth and viability. Our approach overcomes numerous limitations of EM studies, such as alterations in cell shape and CW caused by fixation (Osumi, 2012), and brings the possibility to visualize the CW in a planar section in large populations of living cells. We foresee that this approach could serve as a standard for studying CW function in processes such as growth, reproduction, or infection in bacteria, fungi, or plants, with potential therapeutic values for antifungal and antibiotic chemical screens.

Spatiotemporal CW Dynamics

One important output of our study is to find that CW thickness and mechanics are polarized, with growing poles being typically twice as soft and thin as the rest of the cell. Those mechanical anisotropies, which here derive from internal polarity, have long been speculated to be required for tip elongation and rod-shape morphogenesis (Boudaoud, 2003; Drake and Vavylonis, 2013; Rojas et al., 2011). Patterns of wall elasticity may also influence the morphogenesis of other tip growing cells (Ma et al., 2005; Yanagisawa et al., 2015), as well as that of multicellular plant tissues (Kierzkowski et al., 2012; Milani et al., 2014; Peaucelle et al., 2011). Given the large variety of shapes found in fungal species and mutants, it will be interesting to systematically compare spatial patterns of CW mechanics and thickness with cell shape parameters, to identify generic biomechanical principles guiding the morphogenesis of walled cells. Animal cells also exhibit anisotropic mechanical properties needed for shape changes, cell migration, or tissue morphogenesis, which rest on the organization of internal polarity and cytoskeleton (Levayer and Lecuit, 2012; Mogilner and Keren, 2009). Thus, our data reinforce a concept that morphogenesis may primarily emerge from spatial surface mechanical properties patterned from intracellular biochemical organization.

We also discovered that the CW is highly dynamic at sites of polar growth, with variations in thickness amplitude reaching up to 30% of the mean, on a timescale of tens of minutes. Thickness on cell sides appeared more stable, although we did note some patterns of thickness translating away from cell tip (Videos S1 and S2), plausibly reflecting CW material flowing during cell growth (Abenza et al., 2015). We suggest that thickness fluctuations are indicative of a homeostatic system correcting thickness changes over time, needed to maintain CW

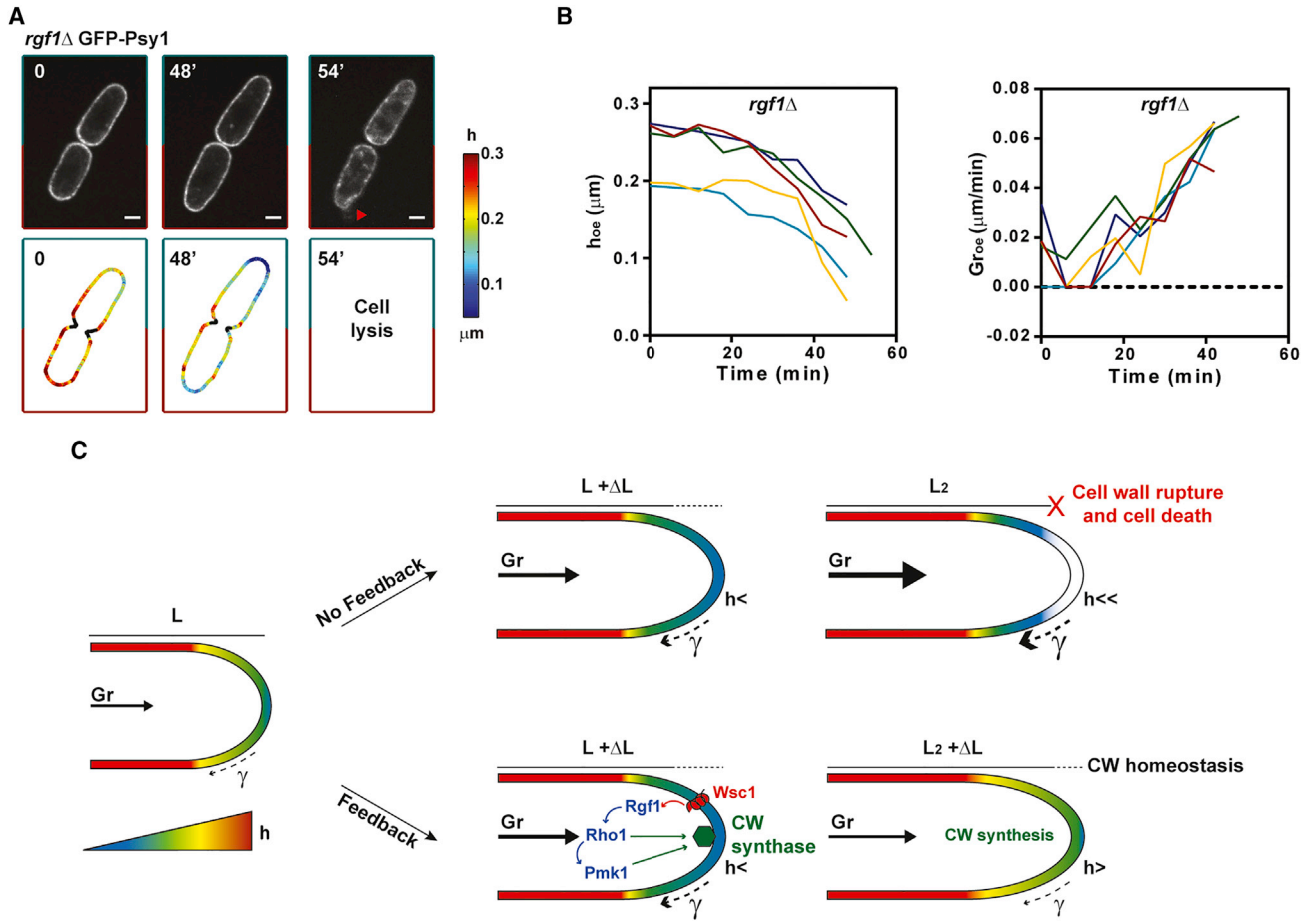

Figure 6. Implication of Thickness Homeostasis for Cell Survival during Normal Growth

(A) Time lapse of GFP-Psy1 and thickness maps for a representative lysing *rgf1Δ* cell. The arrowhead points to membrane leaking at cell tips after lysis.

(B) Evolution of old end thickness (h_{oe}) and growth rates (Gr_{oe}) in lysing *rgf1Δ* cells. The last point is recorded before lysis.

(C) Mechanosensing-based feedback for CW thickness homeostasis during cell growth. In absence of feedback, growth causes CW thinning, which promotes faster growth and further CW thinning, and so on, until the CW ruptures and cells lyse. The CWI pathway probes strain rate (or equivalently growth rates) through the surface protein Wsc1, which promotes the activation (directly or indirectly) of the Rho1-GEF Rgf1 to activate Rho1 and CW synthase. Rgf1 and Rho1 may directly act on synthesis or through the Pmk1 MAPK cascade. As a result, thickness increases, thereby reducing strain rate, yielding to a dynamic homeostatic system for CW mechanical properties and cell integrity. Scale bars, 2 μm.

See also Video S5.

mechanical parameters in an optimal range for growth and viability.

Although the current state of the art precludes dynamically computing changes in elastic moduli in growing cells, we suspect that similar homeostatic systems could also influence composition and bulk elasticity in addition to thickness. CW mechanical oscillations have been speculated to exist in rapidly growing cells such as pollen tubes and fungi, and to be related to cycles of Rho-GTPase activation or calcium signaling and variations in growth rates (Qin and Yang, 2011; Rojas et al., 2011). Fission yeast cells also exhibit oscillations in the abundance of active Cdc42 at cell tips (Das et al., 2012). However, the timescale of those oscillations is typically ten times shorter than that of the CW thickness fluctuations reported here, suggesting those behaviors may not be directly connected in a linear manner in this system. Mechanical fluctuations may thus represent a general readout for negative feedbacks acting at the biochemical or biomechanical level, instrumental to confer robustness to growth and viability (Howell et al., 2012).

Mechanical Homeostasis of the CW by the CWI

By screening through mutants, we uncovered a primary role for specific components of the CWI in probing CW strain and cell growth. Although the role of the CWI in general CW stress response and as a regulator of cell integrity during polar growth had been previously recognized in yeast, fungi, and plants (Banavar et al., 2018; Boisson-Dernier et al., 2013; Levin, 2005; Perez and Cansado, 2010), to our knowledge, those are the very first evidence of its direct role in dynamically controlling CW properties. The implication of Wsc1 in thickness homeostasis and in probing CW mechanical strain to regulate synthase polar domain localization and activity provides significant support that this protein may act as a direct CW mechanical sensor. Wsc1 localizes in patches at cell tips and has a predicted

serine/threonine rich domain spanning the CW (Cruz et al., 2013). It remains a puzzle to understand how such a configuration could directly probe lateral strain in the CW. Studies of *Saccharomyces cerevisiae* orthologs have proposed that WSC clustering may underlie mechanosensory activities (Heinisch et al., 2010). Further work will be needed to understand how those domains may probe the dynamic mechanical properties of the CW. Mutants in the second known fission yeast stress sensor, Mtl2, did not exhibit strong defects in homeostasis, suggesting a dominant function of Wsc1 here. This may be in agreement with the more diffuse localization of Mtl2 all around the cell surface (Cruz et al., 2013). Surprisingly, we found that loss of Rgf2, which has been suggested to physically interact with Wsc1 (Cruz et al., 2013), only had a mild effect on wall thickness homeostasis. *rgf1Δ* mutants exhibited the most pronounced effect, which may account for its severe lysis phenotype. This suggests a potential link between Wsc1 sensing and Rgf1 activation in wall homeostasis and a dominant role for Rgf1p in activating Rho1 in this response (Garcia et al., 2009a). However, we note that 70% of *rgf1Δ* mutant cells still survived, suggesting that a secondary system, likely based on Rgf2, may maintain some form of mechanical homeostasis. Finally, we also found that Pmk1 was required for homeostasis. This suggests that proper homeostasis involves at least partially the expression of a set of regulatory genes for CW construction. This would imply that the Pmk1 cascade acts at short time scales of several minutes, similar to turgor pressure-regulating Sty1/Hog1 MAPK (Miermont et al., 2011). Thus, the dynamic regulation of walled cells' mechanical properties, through rapid adaptation systems, appears as a central element to support viability not only in response to stress but also during normal growth and division (Rojas et al., 2017).

In addition to this homeostatic system protecting single cell thickness dynamics against erratic variations, we also observed thickness variations at the population level on the timescale of 3–4 hr. Although those variations could potentially account for some of the asymmetry in the number of points in certain homeostatic plots, they did not appear to contribute to their global trend (Figure S5). Those two effects were also largely independent: mutants delayed in specific cell cycle phases still exhibited fluctuations and homeostasis, and mutants in CWI components defective in short-term homeostasis displayed similar cell cycle thickness evolution at the population scale as WT (Figures S5H, S5I, and S6C). Further work will be needed to identify the mechanisms driving those large-scale variations, and their potential function.

Growth Control through Mechanochemical Systems

The notion that surface mechanics can alter the core spatiotemporal organization of cells through mechanosensing systems is becoming increasingly important in biology (DuFort et al., 2011). Examples range from the regulation of cell polarity, migration, and cell division up to tissue homeostasis (Bonazzi et al., 2014; Fink et al., 2011; Houk et al., 2012). Here, we uncovered a core function of mechanosensing in growth control. In this view, growth is directly perceived as a mechanical signal straining the CW, without any requirement for interactions with neighboring cells or the cell environment. When a cell begins to elongate rapidly, the strain rate increases, which turns on synthase activation by the CWI to assemble more wall, and vice versa. This homeostatic system thus compensates surface material dilution associated with growth to maintain its thickness around values compatible with survival. As thickness influences elongation rates, this system may also work toward controlling growth rate values around a defined range. Those findings thus have important implications for cell cycle control, as well as size homeostasis, which are both influenced by growth rate values. We speculate that cells may have evolved built-in mechanical properties and sensing elements that allow them to control expansion speeds adapted to their lifestyles. Future work studying similar problems of surface expansion control will inform on how those elements have been modified to guide the growth of rapidly expanding cells such as those in fungi and plants, or slowly growing cells such as those of animals.

STAR★METHODS

Detailed methods are provided in the online version of this paper and include the following:

- KEY RESOURCES TABLE
- CONTACT FOR REAGENT AND RESOURCE SHARING
- EXPERIMENTAL MODEL AND SUBJECT DETAILS
  - Yeast Strains, Media and Genetics
  - Drug Treatments
- METHOD DETAILS
  - Microscopy
  - Transmission Electron Microscopy
  - Microfabricated Channels
  - Turgor Pressure Manipulation by Sorbitol Addition
- QUANTIFICATION AND STATISTICAL ANALYSIS
  - Image Analysis
  - Strain-Stress Assay Simulation
  - Spectrum Analysis of Thickness Fluctuations
  - Analytical Models for Tip Thickness Fluctuations
  - 3D Cell Growth Model
- DATA AND SOFTWARE AVAILABILITY

SUPPLEMENTAL INFORMATION

Supplemental Information includes six figures and five videos and can be found with this article online at https://doi.org/10.1016/j.devcel.2018.03.022.

ACKNOWLEDGMENTS

The authors acknowledge P. Perez, Y. Sanchez, H. Valdivieso, T. Toda, T. Nakamura (YGRC/NBRP Japan), and J.Q. Wu for sharing material. We acknowledge the ImagoSeine core facility of the Institut Jacques Monod, member of IBiSA and France-BioImaging (ANR-10-INBS-04) infrastructures. A.B. is supported by Institut Universitaire de France. The Minc laboratory is supported by the CNRS and grants from the FP7 CIG program (no. 303821), ITN "FungiBrain" (no. 607963), and the European Research Council (CoG Forcaster no. 647073).

AUTHOR CONTRIBUTIONS

V.D., A.H., H.D.B., R.L.B., and N.M. performed experiments. V.D., H.T., D.E., and N.M. developed image analysis scripts. E.C. and A.B. performed modeling. V.D., A.B., and N.M. designed the research and wrote the manuscript.

DECLARATION OF INTERESTS

A patent on this method was deposited under the number FR1657801 on August 17, 2016.

Received: October 11, 2017
Revised: February 5, 2018
Accepted: March 26, 2018
Published: April 23, 2018

REFERENCES

Abenza, J.F., Couturier, E., Dodgson, J., Dickmann, J., Chessel, A., Dumais, J., and Carazo Salas, R.E. (2015). Wall mechanics and exocytosis define the shape of growth domains in fission yeast. Nat. Commun. *6*, 8400.

Arellano, M., Durán, A., and Pérez, P. (1996). Rho 1 GTPase activates the (1-3) beta-D-glucan synthase and is involved in *Schizosaccharomyces pombe* morphogenesis. EMBO J. *15*, 4584–4591.

Arellano, M., Valdivieso, M.H., Calonge, T.M., Coll, P.M., Duran, A., and Perez, P. (1999). *Schizosaccharomyces pombe* protein kinase C homologues, pck1p and pck2p, are targets of rho1p and rho2p and differentially regulate cell integrity. J. Cell Sci. *112* (Pt 20), 3569–3578.

Atilgan, E., Magidson, V., Khodjakov, A., and Chang, F. (2015). Morphogenesis of the fission yeast cell through cell wall expansion. Curr. Biol. *25*, 2150–2157.

Banavar, S.P., Gomez, C., Trogdon, M., Petzold, L.R., Yi, T.M., and Campas, O. (2018). Mechanical feedback coordinates cell wall expansion and assembly in yeast mating morphogenesis. PLoS Comput. Biol. *14*, e1005940.

Bastmeyer, M., Deising, H.B., and Bechinger, C. (2002). Force exertion in fungal infection. Annu. Rev. Biophys. Biomol. Struct. *31*, 321–341.

Bendezu, F.O., and Martin, S.G. (2011). Actin cables and the exocyst form two independent morphogenesis pathways in the fission yeast. Mol. Biol. Cell *22*, 44–53.

Boisson-Dernier, A., Lituiev, D.S., Nestorova, A., Franck, C.M., Thirugnanarajah, S., and Grossniklaus, U. (2013). ANXUR receptor-like kinases coordinate cell wall integrity with growth at the pollen tube tip via NADPH oxidases. PLoS Biol. *11*, e1001719.

Bonazzi, D., Haupt, A., Tanimoto, H., Delacour, D., Salort, D., and Minc, N. (2015). Actin-based transport adapts polarity domain size to local cellular curvature. Curr. Biol. *25*, 2677–2683.

Bonazzi, D., Julien, J.D., Romao, M., Seddiki, R., Piel, M., Boudaoud, A., and Minc, N. (2014). Symmetry breaking in spore germination relies on an interplay between polar cap stability and spore wall mechanics. Dev. Cell *28*, 534–546.

Boudaoud, A. (2003). Growth of walled cells: from shells to vesicles. Phys. Rev. Lett. *91*, 018104.

Cassone, A., Kerridge, D., and Gale, E.F. (1979). Ultrastructural changes in the cell wall of *Candida albicans* following cessation of growth and their possible relationship to the development of polyene resistance. J. Gen. Microbiol. *110*, 339–349.

Chang, F., and Huang, K.C. (2014). How and why cells grow as rods. BMC Biol. *12*, 54.

Chang, F., and Martin, S.G. (2009). Shaping fission yeast with microtubules. Cold Spring Harb. Perspect. Biol. *1*, a001347.

Charvin, G., Cross, F.R., and Siggia, E.D. (2008). A microfluidic device for temporally controlled gene expression and long-term fluorescent imaging in unperturbed dividing yeast cells. PLoS One *3*, e1468.

Chugh, P., Clark, A.G., Smith, M.B., Cassani, D.A.D., Dierkes, K., Ragab, A., Roux, P.P., Charras, G., Salbreux, G., and Paluch, E.K. (2017). Actin cortex architecture regulates cell surface tension. Nat. Cell Biol. *19*, 689–697.

Clark, A.G., Dierkes, K., and Paluch, E.K. (2013). Monitoring actin cortex thickness in live cells. Biophys. J. *105*, 570–580.

Cortes, J.C., Carnero, E., Ishiguro, J., Sanchez, Y., Duran, A., and Ribas, J.C. (2005). The novel fission yeast (1,3)beta-D-glucan synthase catalytic subunit Bgs4p is essential during both cytokinesis and polarized growth. J. Cell Sci. *118*, 157–174.

Cosgrove, D.J. (2005). Growth of the plant cell wall. Nat. Rev. Mol. Cell Biol. *6*, 850–861.

Cruz, S., Muñoz, S., Manjón, E., García, P., and Sanchez, Y. (2013). The fission yeast cell wall stress sensor-like proteins Mtl2 and Wsc1 act by turning on the GTPase Rho1p but act independently of the cell wall integrity pathway. Microbiologyopen *2*, 778–794.

Dagdas, Y.F., Yoshino, K., Dagdas, G., Ryder, L.S., Bielska, E., Steinberg, G., and Talbot, N.J. (2012). Septin-mediated plant cell invasion by the rice blast fungus, *Magnaporthe oryzae*. Science *336*, 1590–1595.

Das, M., Drake, T., Wiley, D.J., Buchwald, P., Vavylonis, D., and Verde, F. (2012). Oscillatory dynamics of Cdc42 GTPase in the control of polarized growth. Science *337*, 239–243.

Das, M., Wiley, D.J., Chen, X., Shah, K., and Verde, F. (2009). The conserved NDR kinase Orb6 controls polarized cell growth by spatial regulation of the small GTPase Cdc42. Curr. Biol. *19*, 1314–1319.

Das, M., Wiley, D.J., Medina, S., Vincent, H.A., Larrea, M., Oriolo, A., and Verde, F. (2007). Regulation of cell diameter, For3p localization, and cell symmetry by fission yeast Rho-GAP Rga4p. Mol. Biol. Cell *18*, 2090–2101.

Davi, V., and Minc, N. (2015). Mechanics and morphogenesis of fission yeast cells. Curr. Opin. Microbiol. *28*, 36–45.

Davidson, R., Laporte, D., and Wu, J.Q. (2015). Regulation of Rho-GEF Rgf3 by the arrestin Art1 in fission yeast cytokinesis. Mol. Biol. Cell *26*, 453–466.

DeBerardinis, R.J., Lum, J.J., Hatzivassiliou, G., and Thompson, C.B. (2008a). The biology of cancer: metabolic reprogramming fuels cell growth and proliferation. Cell Metab. *7*, 11–20.

Deberardinis, R.J., Sayed, N., Ditsworth, D., and Thompson, C.B. (2008b). Brick by brick: metabolism and tumor cell growth. Curr. Opin. Genet. Dev. *18*, 54–61.

Drake, T., and Vavylonis, D. (2013). Model of fission yeast cell shape driven by membrane-bound growth factors and the cytoskeleton. PLoS Comput. Biol. *9*, e1003287.

Dudin, O., Bendezu, F.O., Groux, R., Laroche, T., Seitz, A., and Martin, S.G. (2015). A formin-nucleated actin aster concentrates cell wall hydrolases for cell fusion in fission yeast. J. Cell Biol. *208*, 897–911.

DuFort, C.C., Paszek, M.J., and Weaver, V.M. (2011). Balancing forces: architectural control of mechanotransduction. Nat. Rev. Mol. Cell Biol. *12*, 308–319.

Fantes, P., and Nurse, P. (1977). Control of cell size at division in fission yeast by a growth-modulated size control over nuclear division. Exp. Cell Res. *107*, 377–386.

Fink, J., Carpi, N., Betz, T., Betard, A., Chebah, M., Azioune, A., Bornens, M., Sykes, C., Fetler, L., Cuvelier, D., et al. (2011). External forces control mitotic spindle positioning. Nat. Cell Biol. *13*, 771–778.

Flor-Parra, I., Zhurinsky, J., Bernal, M., Gallardo, P., and Daga, R.R. (2014). A Lallzyme MMX-based rapid method for fission yeast protoplast preparation. Yeast *31*, 61–66.

Garcia, P., Garcia, I., Marcos, F., de Garibay, G.R., and Sanchez, Y. (2009a). Fission yeast rgf2p is a rho1p guanine nucleotide exchange factor required for spore wall maturation and for the maintenance of cell integrity in the absence of rgf1p. Genetics *181*, 1321–1334.

Garcia, P., Tajadura, V., Garcia, I., and Sanchez, Y. (2006). Rgf1p is a specific Rho1-GEF that coordinates cell polarization with cell wall biogenesis in fission yeast. Mol. Biol. Cell *17*, 1620–1631.

Garcia, P., Tajadura, V., and Sanchez, Y. (2009b). The Rho1p exchange factor Rgf1p signals upstream from the Pmk1 mitogen-activated protein kinase pathway in fission yeast. Mol. Biol. Cell *20*, 721–731.

Harold, F.M. (2002). Force and compliance: rethinking morphogenesis in walled cells. Fungal Genet. Biol. *37*, 271–282.

Harris, L.K., and Theriot, J.A. (2016). Relative rates of surface and volume synthesis set bacterial cell size. Cell *165*, 1479–1492.

Heinisch, J.J., Dupres, V., Wilk, S., Jendretzki, A., and Dufrene, Y.F. (2010). Single-molecule atomic force microscopy reveals clustering of the yeast plasma-membrane sensor Wsc1. PLoS One *5*, e11104.

Hepler, P.K., Vidali, L., and Cheung, A.Y. (2001). Polarized cell growth in higher plants. Annu. Rev. Cell Dev. Biol. *17*, 159–187.

Holley, R.W. (1975). Control of growth of mammalian cells in cell culture. Nature *258*, 487–490.

Hong, L., Dumond, M., Tsugawa, S., Sapala, A., Routier-Kierzkowska, A.L., Zhou, Y., Chen, C., Kiss, A., Zhu, M., Hamant, O., et al. (2016). Variable cell growth yields reproducible organ development through spatiotemporal averaging. Dev. Cell *38*, 15–32.

Horiseberger, M., and Rosset, J. (1977). Localization of alpha-Galactomannan on the surface of *Schizosaccharomyces pombe* cells by scanning electron microscopy. Arch. Microbiol. *112*, 123–126.

Houk, A.R., Jilkine, A., Mejean, C.O., Boltyanskiy, R., Dufresne, E.R., Angenent, S.B., Altschuler, S.J., Wu, L.F., and Weiner, O.D. (2012). Membrane tension maintains cell polarity by confining signals to the leading edge during neutrophil migration. Cell *148*, 175–188.

Howell, A.S., Jin, M., Wu, C.F., Zyla, T.R., Elston, T.C., and Lew, D.J. (2012). Negative feedback enhances robustness in the yeast polarity establishment circuit. Cell *149*, 322–333.

Huang, S., and Ingber, D.E. (1999). The structural and mechanical complexity of cell-growth control. Nat. Cell Biol. *1*, E131–E138.

Keegstra, K. (2010). Plant cell walls. Plant Physiol. *154*, 483–486.

Kelly, F.D., and Nurse, P. (2011). De novo growth zone formation from fission yeast spheroplasts. PLoS One *6*, e27977.

Kierzkowski, D., Nakayama, N., Routier-Kierzkowska, A.L., Weber, A., Bayer, E., Schorderet, M., Reinhardt, D., Kuhlemeier, C., and Smith, R.S. (2012). Elastic domains regulate growth and organogenesis in the plant shoot apical meristem. Science *335*, 1096–1099.

Lander, A.D. (2011). Pattern, growth, and control. Cell *144*, 955–969.

Levayer, R., and Lecuit, T. (2012). Biomechanical regulation of contractility: spatial control and dynamics. Trends Cell Biol. *22*, 61–81.

Levin, D.E. (2005). Cell wall integrity signaling in *Saccharomyces cerevisiae*. Microbiol. Mol. Biol. Rev. *69*, 262–291.

Lew, R.R. (2011). How does a hypha grow? The biophysics of pressurized growth in fungi. Nat. Rev. Microbiol. *9*, 509–518.

Lipke, P.N., and Ovalle, R. (1998). Cell wall architecture in yeast: new structure and new challenges. J. Bacteriol. *180*, 3735–3740.

Ma, H., Snook, L.A., Kaminskyj, S.G., and Dahms, T.E. (2005). Surface ultrastructure and elasticity in growing tips and mature regions of *Aspergillus* hyphae describe wall maturation. Microbiology *151*, 3679–3688.

Mahadevan, L., and Mitchison, T.J. (2005). Cell biology: powerful curves. Nature *435*, 895–897.

Marshall, W.F., Young, K.D., Swaffer, M., Wood, E., Nurse, P., Kimura, A., Frankel, J., Wallingford, J., Walbot, V., Qu, X., et al. (2012). What determines cell size? BMC Biol. *10*, 101.

Martins, I.M., Cortes, J.C., Munoz, J., Moreno, M.B., Ramos, M., Clemente-Ramos, J.A., Duran, A., and Ribas, J.C. (2011). Differential activities of three families of specific beta(1,3)glucan synthase inhibitors in wild-type and resistant strains of fission yeast. J. Biol. Chem. *286*, 3484–3496.

Mata, J., and Nurse, P. (1997). tea1 and the microtubular cytoskeleton are important for generating global spatial order within the fission yeast cell. Cell *89*, 939–949.

McKenna, S.T., Kunkel, J.G., Bosch, M., Rounds, C.M., Vidali, L., Winship, L.J., and Hepler, P.K. (2009). Exocytosis precedes and predicts the increase in growth in oscillating pollen tubes. Plant Cell *21*, 3026–3040.

Miermont, A., Uhlendorf, J., McClean, M., and Hersen, P. (2011). The dynamical systems properties of the HOG signaling cascade. J. Signal Transduct. *2011*, 930940.

Milani, P., Mirabet, V., Cellier, C., Rozier, F., Hamant, O., Das, P., and Boudaoud, A. (2014). Matching patterns of gene expression to mechanical stiffness at cell resolution through quantitative tandem epifluorescence and nanoindentation. Plant Physiol. *165*, 1399–1408.

Minc, N., Boudaoud, A., and Chang, F. (2009). Mechanical forces of fission yeast growth. Curr. Biol. *19*, 1096–1101.

Mitchison, J.M., and Nurse, P. (1985). Growth in cell length in the fission yeast *Schizosaccharomyces pombe*. J. Cell Sci. *75*, 357–376.

Mogilner, A., and Keren, K. (2009). The shape of motile cells. Curr. Biol. *19*, R762–R771.

Muñoz, J., Cortés, J.C., Sipiczki, M., Ramos, M., Clemente-Ramos, J.A., Moreno, M.B., Martins, I.M., Peréz, P., and Ribas, J.C. (2013). Extracellular cell wall beta(1,3)glucan is required to couple septation to actomyosin ring contraction. J. Cell Biol. *203*, 265–282.

Murray, S. (2008). High pressure freezing and freeze substitution of *Schizosaccharomyces pombe* and *Saccharomyces cerevisiae* for TEM. Methods Cell Biol. *88*, 3–17.

Mutoh, T., Nakano, K., and Mabuchi, I. (2005). Rho1-GEFs Rgf1 and Rgf2 are involved in formation of cell wall and septum, while Rgf3 is involved in cytokinesis in fission yeast. Genes Cells *10*, 1189–1202.

Nakamura, T., Nakamura-Kubo, M., Hirata, A., and Shimoda, C. (2001). The *Schizosaccharomyces pombe* spo3+ gene is required for assembly of the forespore membrane and genetically interacts with psy1(+)-encoding syntaxin-like protein. Mol. Biol. Cell *12*, 3955–3972.

Nakayama, N., Smith, R.S., Mandel, T., Robinson, S., Kimura, S., Boudaoud, A., and Kuhlemeier, C. (2012). Mechanical regulation of auxin-mediated growth. Curr. Biol. *22*, 1468–1476.

Novick, P., and Schekman, R. (1979). Secretion and cell-surface growth are blocked in a temperature-sensitive mutant of *Saccharomyces cerevisiae*. Proc. Natl. Acad. Sci. USA *76*, 1858–1862.

Osumi, M. (2012). Visualization of yeast cells by electron microscopy. J. Electron Microsc. (Tokyo) *61*, 343–365.

Peaucelle, A., Braybrook, S.A., Le Guillou, L., Bron, E., Kuhlemeier, C., and Hofte, H. (2011). Pectin-induced changes in cell wall mechanics underlie organ initiation in *Arabidopsis*. Curr. Biol. *21*, 1720–1726.

Perez, P., and Cansado, J. (2010). Cell integrity signaling and response to stress in fission yeast. Curr. Protein Pept. Sci. *11*, 680–692.

Perez, P., and Ribas, J.C. (2004). Cell wall analysis. Methods *33*, 245–251.

Petersen, J., Heitz, M.J., and Hagan, I.M. (1998). Conjugation in *S. pombe*: identification of a microtubule-organising centre, a requirement for microtubules and a role for Mad2. Curr. Biol. *8*, 963–966.

Qin, Y., and Yang, Z. (2011). Rapid tip growth: insights from pollen tubes. Semin. Cell Dev. Biol. *22*, 816–824.

Rojas, E., Theriot, J.A., and Huang, K.C. (2014). Response of *Escherichia coli* growth rate to osmotic shock. Proc. Natl. Acad. Sci. USA *111*, 7807–7812.

Rojas, E.R., Hotton, S., and Dumais, J. (2011). Chemically mediated mechanical expansion of the pollen tube cell wall. Biophys. J. *101*, 1844–1853.

Rojas, E.R., Huang, K.C., and Theriot, J.A. (2017). Homeostatic cell growth is accomplished mechanically through membrane tension inhibition of cell-wall synthesis. Cell Syst. *5*, 578–590.e6.

Salbreux, G., Charras, G., and Paluch, E. (2012). Actin cortex mechanics and cellular morphogenesis. Trends Cell Biol. *22*, 536–545.

Silhavy, T.J., Kahne, D., and Walker, S. (2010). The bacterial cell envelope. Cold Spring Harb. Perspect. Biol. *2*, a000414.

Tatebe, H., Nakano, K., Maximo, R., and Shiozaki, K. (2008). Pom1 DYRK regulates localization of the Rga4 GAP to ensure bipolar activation of Cdc42 in fission yeast. Curr. Biol. *18*, 322–330.

Thompson, B.J. (2010). Developmental control of cell growth and division in *Drosophila*. Curr. Opin. Cell Biol. *22*, 788–794.

Villar-Tajadura, M.A., Coll, P.M., Madrid, M., Cansado, J., Santos, B., and Perez, P. (2008). Rga2 is a Rho2 GAP that regulates morphogenesis and cell integrity in *S. pombe*. Mol. Microbiol. *70*, 867–881.

Yanagisawa, M., Desyatova, A.S., Belteton, S.A., Mallery, E.L., Turner, J.A., and Szymanski, D.B. (2015). Patterning mechanisms of cytoskeletal and cell wall systems during leaf trichome morphogenesis. Nat. Plants *1*, 15014.

Zegman, Y., Bonazzi, D., and Minc, N. (2015). Measurement and manipulation of cell size parameters in fission yeast. Methods Cell Biol. *125*, 423–436.

STAR★METHODS

KEY RESOURCES TABLE

REAGENT or RESOURCE	SOURCE	IDENTIFIER
Experimental Models: Organisms/Strains		
h- *cut11-RFP:HygR GFP-psy1:leu* (*leu1-32 ura4-D18*)	This study	VD11
h- *CRIB-tdTomato:ura GFP-psy1:leu* (*leu1-32 ura4-D18*)	This study	VD20
h- *tea1::NatMX CRIB-tdTomato:ura GFP-psy1:leu* (*leu1-32 ura4-D18)*	This study	VD31
h+*CRIB-tdTomato:ura GFP-psy1:leu* (*leu1-32 ura4-D18*)	This study	VD39
h- *CRIB-tdTomato:ura GFP-psy1:leu orb6-25* (*leu1-32 ura4-D18*)	This study	VD50
h+ *GFP-psy1:ade bgs4::ura4 RFP-bgs4-Leu* (*leu1-32 ura4-D18 ade6*)	This study	VD57
h- *GFP-psy1:ade bgs4::ura4 RFP-bgs4-Leu Leu* (*leu1-32 ura4-D18 ade6*)	This study	VD58
h- *rga2::KanMX bgs4::ura4 RFP-bgs4-Leu GFP-psy1:ade* (*leu1-32 ura4-D18*)	This study	VD72
h- *rga4::KanMX bgs4::ura4 RFP-bgs4-Leu GFP-psy1:ade* (*leu1-32 ura4-D18*)	This study	VD81
h- *GFP-psy1:ade pREP3X-pck2* (*leu1-32 ade6*)	This study	VD93
h- *GFP-psy1:ade pRep3X empty vector* (*leu1-32 ade6*)	This study	VD105
h+ *GFP-psy1:ade pRep3X-rho1G15V*	This study	VD69
h- *tea1::NatMX GFP-psy1:ade bgs4::ura4 RFP-bgs4:leu* (*leu1-32 ura4-D18 ade6*)	This study	VD110
h- cwg1-1 GFP-psy1:leu CRIB-tdTomato:ura (*leu1-32 ura4-D18*)	This study	VD115
h+ wsc1::KanMX GFP-psy1:ade bgs4::ura4 RFP-bgs4:leu (*leu1-32 ura4-D18 ade6*)	This study	VD158
h- mtl2::KanMX GFP-psy1:ade bgs4::ura4 RFP-bgs4:leu (*leu1-32 ura4-D18 ade6*)	This study	VD160
h^{90} *rga4::KanMX GFP-psy1:ade bgs4::ura4 RFP-bgs4:leu* (*leu1-32 ura4-D18 ade6*)	This study	VD162
h- *pck2 :leu GFP-psy1:ade*	This study	VD109
h+ rgf2::ura GFP-psy1:ade (*leu1-32 ura4-D18 ade6*)	This study	VD164
h+ *rgf1::KanMX GFP-psy1:ade* (*leu1-32 ura4-D18 ade6*)	This study	VD167
h+ pmk1:ura GFP-psy1:leu (*leu1-32 ura4-D18*)	This study	VD173
h+ *pRep3X-Phluorin-ritc* (*leu1-32*)	This study	NM164
h+ *Leu:GFP-psy1* (*leu1-32 ura4-D18*)	This study	NM468
h- *Leu:GFP-psy1* (*leu1-32 ura4-D18*)	This study	NM469
h+ *shk1:GFP-LactC2:leu*	This study	AH159
h+ *shk1:GFP-8+:leu (ura4-D18 ade6*)	This study	AH208
h+ gpd1::NatMX GFP-bgs4:leu bgs4::ura (*leu1-32 ura4-D18 ade6*)	This study	NM266
h- gpd1::NatMX wsc1::KanMX GFP-bgs4:leu bgs4::ura (*ade6*)	This study	AH330
h- *gpd1::NatMX P3nmt1-pkc1(HR1-C2)-ECitrine* (*ura4-D18*)	This study	AH385
h- gpd1::NatMX wsc1::KanMX P3nmt1-pkc1(HR1-C2)-ECitrine (*leu1-32 ura4-D18 ade6*)	This study	AH401
h+ *cdc10-M17 GFP-psy1:ade bgs4::ura4 RFP-bgs4-Leu (ade6)*	This study	VD122
h- *cdc25-22 GFP-psy1:ade bgs4::ura4 RFP-bgs4-Leu* (*leu1-32 ura4-D18 ade6*)	This study	VD123
Chemicals, Peptides, and Recombinant Proteins		
Zymolyase	ZymoResearch	E1004
LatrunculinA	Sigma-Aldrich	L5163
Caspofungin	Sigma-Aldrich	SML0425
Gs-IB_4 -Alexafluor647	ThermoFisher	I32450
Bs-IB4-TRIC	Sigma-Aldrich	N/A

CONTACT FOR REAGENT AND RESOURCE SHARING

Further information and requests for resources and reagents should be directed to and will be fulfilled by the Lead Contact, Nicolas Minc (nicolas.minc@ijm.fr).

EXPERIMENTAL MODEL AND SUBJECT DETAILS

Yeast Strains, Media and Genetics

Standard methods for *Schizosaccharomyces pombe* media and genetic manipulations were used (http://www-bcf.usc.edu/~forsburg/). Strains used in this study are listed in Key Resource Table below. Cells were grown at 25°C in yeast extract plus 5 supplements (YE5S) media unless otherwise indicated. Over-expression driven from plasmids, was induced by growing cells at 25°C in Edinburgh minimal medium (EMM) + supplements without thiamine for 24-36 h for Pck2, Rho1-G15V, and 48h for the membrane probe GFP-RITC and for ActRho1-Cit. Starvation of wild-type (wt) cells was induced by over-growing cells in liquid YE5S for an additional 16 h after they had reached stationary phase (OD_{600}>1). Recovery from starvation in *tea1Δ* cells was induced by growing cells on YE5S plates for > 3 days, and subsequently transferring them in YE5S liquid media for 2-3h before observation or directly on 2% YE5S agar pads for time lapse. Temperature sensitive alleles, *cwg1-1*, *orb6-25, cdc25-22* and *cdc10-M17* were grown in liquid culture at permissive temperature (25°C) and switched to restrictive temperature (36°C) for 6h, 2h, 1h and 3h respectively, before observation. Spores were obtained from homothallic h90 strains, or from heterothallic crosses. Freshly growing cells were placed on malt extract (ME) solid media for 3 days. Mating mixtures were then digested for 1h at room temperature in a 1/200 glusulase solution in water to kill vegetative cells, washed three times in water, and incubated for >7h in YE5S before observation (Bonazzi et al., 2014). Spheroplasts were generated from exponentially growing cells in YE5S, which were washed twice in digestion buffer (0.1M Citric Acid 0.1 M NaCitrate pH = 5.8; 1.2 M Sorbitol) and subsequently treated with Lallzyme (0.1 g/ml) during 1h at room temperature. Newly formed spheroplasts, were washed twice in YE5S+1.2 M Sorbitol, and let to regenerate at 25°C for >16h, until outgrowing protrusions appeared (Flor-Parra et al., 2014). To image mating protrusions, homothallic cells growing exponentially in liquid YE5S were placed on solid ME until mating protrusion appeared (>5h). Cells were then harvested, labeled and imaged directly.

Drug Treatments

Cell wall digestion was achieved by incubating cells with 5000U/ml Zymolyase (ZymoResearch) at room temperature, and imaged immediately after treatment and 1h after. LatrunculinA (Sigma) was used at a final concentration of 100 μM from a 100X stock in DMSO. Cells were incubated for 30' at room temperature before imaging. For Caspofungin experiments, cells were plated on 2% agar pads made with YE5S+10 mg/ml *Gs*-IB_4 -Alexafluor647 and a final concentration of 5μM Caspofungin.

METHOD DETAILS

Microscopy

Live-cell imaging was performed on two different inverted spinning-disk confocal microscopes equipped with motorized stages, automatic focus and controlled with MetaMorph® (Microscopy Automation & Image Analysis Software). The first one (Nikon Ti-Eclipse), is equipped with a Yokogawa CSU-X1FW spinning head, and an EM-CCD camera (Hamamatsu), a 100× oil-immersion objective (Nikon CFI Plan Apo DM 100×/1.4 NA) and a 2.5× magnifying lens, yielding a pixel size of 43 nm. The second one (Leica DMI8), is equipped with a Yokogawa CSU-W1 spinning head, and a sCMOS Orca-Flash 4 V2+ (Hamamatsu) a 100× oil-immersion objective (Leica Plan Apo DM 100×oil/1.4 NA), yielding a pixel size of 70 nm.

Image registration was performed by imaging a slide containing a solution of 0.2 μm TetraSpeck™ microspheres (Thermofisher). A field containing one bead, was moved sequentially using the Metamorph function "ScanStage" coupled with a home built plugin to allow multi-dimensional acquisition. This generated an array of fluorescent spots imaged at multiple wavelength, for image registration (Figure S1A, see below). Alternatively, single images of a dense field of non-aggregated beads, could be used to generate the vectorial map.

For cell wall thickness measurements, cells were pre-labeled in growth media containing 5 μg/ml of labelled lectin from *Griffonia simplicifolia* (alias *Bandeiraea simplicifolia*) *Gs*-IB_4-Alexafluor647 or *Bs*-IB_4-TRIC (Horiseberger and Rosset, 1977). For single-time imaging, cells were placed between a glass slide and a coverslip and imaged within 20 min. For time-lapse imaging, cells were placed on 2% agar-pads made of YE5S containing 10 μg/ml *Gs*-IB_4-Alexafluor647 and covered with a coverslip. We detected small differences in thickness between experiments performed in glass slides (202±19 nm, n=169) and in agar pads (177±28 nm, n=66), with glass slides generally yielding thicker values, which could be attributed to small cell deformation or starvation. For this reason, all experiments done in mutants, drugs or by modifying protocols are associated with a control measured in the same manner. Comparison with electron microscopy was performed on agar pads. Imaging was generally performed at room temperature (22-26°C), with controlled humidity (>30%). For temperature-sensitive mutants, the temperature of the sample was kept at 36°C by using either a temperature controlled cage or an objective heater (Bioptechs).

Transmission Electron Microscopy

For high pressure freezing (Figure 1B), cells were grown in liquid and harvested on a vacuum filter. The pellets were transferred to 100μm deep flat carriers (Leica Microsystems). Samples were then cryo-immobilized by HPF (EM-Pact2, Leica microsystems). Freeze substitution was performed with an AFS2 (Leica Microsystems) in 2% Osmium, 0,1% Uranyl acetate in pure acetone following protocols described in (Murray, 2008). Samples were rinsed three times with acetone and infiltrated with gradually increasing

concentrations of an Epon resin mix (Agar scientific) and polymerized for 24h at 60°C. Ultrathin (70 nm) sections were generated with an ultramicrotome (UC6, Leica Microsystems) and collected on formvar/carbon-coated grids. Sections were post-stained by aqueous 2% uranyl acetate and lead citrate before imaging.

For chemical fixation (Figure 1B), samples were fixed with 2% glutaraldehyde in Phosphate Buffer 0.2M buffer, for 1h at room temperature followed by overnight fixation at 4°C and post-fixed with 2% osmium tetroxide in water. Samples were dehydrated through a graded series of ethanol and propylene oxide and embedded in epoxy resin. Ultrathin (70 nm) sections were generated with an ultramicrotome (UC6, Leica Microsystems) and collected on formvar/carbon-coated copper grids. Sections were then post-stained by aqueous 4% uranyl acetate and lead citrate.

For Correlative Light Electron Microscopy (CLEM), cells were immobilized on specialized bottom glass petri-dish with micro-grids for image position registrations (MatTek) (Figure S2D). Dishes were pre-treated with 1 mg/ml poly-lysine, followed by 0.1 mg/ml *Bs*-IB_4-lectin and rinsed with water and YE5S. Cells, pre-labeled with *Gs*-IB_4-Alexafluor647, were placed on the dish, let to sediment and stick for ~15 min, and were subsequently rinsed vigorously with YE5S to detach non-sticking cells. Cells were then fixed with 2% glutaraldehyde in YE5S media for 2h at 4°C. Cells were then imaged in light microscopy and their positions were recorded using marks on the micro-grid. The samples were post-fixed with 2% osmium tetroxide in water and dehydrated through a graded series of ethanol and embedded in epoxy resin, which tends to stick to the micro-grid. Ultrathin (70 nm) sections of selected regions of the micro-grid, were generated with an ultramicrotome (Ultracut UC6, Leica) and collected on formvar/carbon-coated copper grids. Sections were then post-stained by aqueous 4% uranyl acetate and lead citrate. We observed often a partial cell deformation recorded in TEM, plausibly due to resin embedding. In spite of this, the cell wall remained intact in most cases. All samples were observed in a Tecnai12 (FEI, The Netherlands) transmission electron microscope at 80 kV equipped with a 1K×1K Keen View camera.

Microfabricated Channels

Microchannels used to manipulate cell diameter, were fabricated in PDMS from a silicon wafer using classical soft-lithography procedures, as described in (Zegman et al., 2015) (Figure 3H). Homothallic *rga4Δ* spores were inserted into the PDMS microchannels, let to germinate for >20h at 25°C, and subsequently rinsed with YE5S + *Gs*-IB_4 -Alexafluor647 for 2h before imaging.

Turgor Pressure Manipulation by Sorbitol Addition

For sorbitol treatments cells were pre-labeled in growth media containing 5 μg/ml of labelled lectin *Gs*-IB_4 -Alexafluor647, then placed in PDMS microfluidic chambers between a dialysis membrane and a coverslip, which allowed live fluid exchange (Charvin et al., 2008). Cells were left in the chamber 40 minutes for adaptation before starting the assay. For Young modulus estimations cells were imaged, then immediately rinsed in the same media containing 1.5 M sorbitol and imaged again within the next 4 minutes. For growth rate manipulation, cells were imaged every 2 minutes for 10 minutes in YE5S + *Gs*-IB_4-Alexafluor647, then washed in the same media containing 0.5M Sorbitol and imaged for 30-60 minutes. In this context, we noted that the induced ActRho1-Cit strain exhibited higher growth rate than unlabeled controls, suggesting some putative levels of non-functionality of the probe (Figure S4H).

QUANTIFICATION AND STATISTICAL ANALYSIS

Image Analysis

Cell Wall Thickness Measurement

The analysis pipeline to compute CW thickness was fully automated with a manual check option at each step. All the analyses were performed using custom scripts written in MATLAB (Mathworks, R2013a equipped with Image Processing and Statistics toolboxes). Initial cell segmentation was performed using either fluorescent membrane or lectin signals. The signal was first binarized using a threshold determined with the graythresh function. The cell contour was defined as the most outer set of pixels of the binarized signal. The coordinates corresponding to the points along the cell contour were then equally spaced with an interval of 1 pixel using a spline function. Typically, a single cell contour was represented by ~ 600-800 points for a pixel size of 43 nm. At each point of the contour, a 40 pixels long line perpendicular to the cell contour was defined as the normal to the tangent of the curve determined using 11 neighboring points (Figure 1A first panel, blue line). The membrane and lectin signals were scanned along these lines, leading to one dimensional intensity profiles for each signal at each position around the cell contour (Figure 1A second panel). The center of each intensity profile was identified by fitting a Gaussian function on 11 points around the point with maximum intensity. Each of these centers defined the XY coordinates of membrane and lectin along the contour of the cell. To correct for chromatic shifts, the coordinates of the wall were changed using the position-dependent chromatic shift vectorial map (Figure S1A, see next section). This first set of analyses defines the precise in-plane coordinates of both outlines of cell membrane and lectin signals (Figure 1A, third panel). Subsequently, novel lines perpendicular to the lectin boundary spaced by 1pixel were defined, following the same procedure as above (In Figure 1A second panel, only 1 out 10 of those lines are drawn, for clarity). The position of the cell membrane along the normal lines was defined as the intersection point between the normal line and the cell membrane. Finally, the local cell wall thickness h was computed as the distance between lectin and membrane coordinates along the normal line (Figure 1A third panel insert). Lateral resolution was estimated based on the lateral precision with which we could detect birth scars (~500 nm) (Figure 1A fourth panel, Figures 1C and S2E–S2G).

Chromatic Shift Correction

To correct for chromatic positional XY shifts between the channels used for the lectin and membrane signals across the field of view we used a ''point-by-point correction'' approach. In contrast to standard ''whole image'' alignment approaches (Clark et al., 2013), this produces a continuous vector field containing shifts for all pixels in the field of view, and can thus account for non-uniformity in the positional drift. Starting from arrays of 200 nm beads imaged at different wavelengths (see above), we first detect the particles positions with a sub-pixel precision (~20-25 nm) using a modified Matlab script available from M. Kilfoil lab (http://people.umass.edu/kilfoil/). The positions of the particles in the two channels (X1, Y1) and (X2, Y2) were then used to compute a sparse map of point-by-point shift vectors, defined as: V = (Vx, Vy) = (X2 – X1, Y2 – Y1) (with one channel used as the reference and features in the second one being aligned) (Figure S1A right panel). This sparse array was then used to generate a continuous point-by-point shift map. For this, each of the two 3-dimentional sets of data: (X1, Y1, Vx) and (X1, Y1, Vy) were fitted with a plane, which allows for computing a point-to-point shift vector Vi at any position (Xi, Yi) with a sub-pixel resolution close to the particle center detection limit (~20-25 nm) (Figure S1A). This map was finally used as an input in the cell wall thickness measurement scripts described above (Figure S1C).

To assess chromatic shifts in Z, we imaged a 3 μm deep Z stack with 10 nm spacing between slices of the same 200 nm beads in 5 different positions in the field of view in two wavelengths channels. To reproduce the distance of the cell center from the cover glass (about 2 μm), beads were embedded in 2% agar pad, and only beads at about 2 μm from the glass surface were imaged. For each stack the fluorescent peaks were detected using a Gaussian fit, and the shifts computed from the distance between the peaks. We found that this shift ranged typically from 0.1 to 0.4 μm, which corresponds to a maximum projected shift in thickness smaller than 30 nm that we neglected for the measurement (Figure S1B).

Generation and Analysis of Simulated Images

Simulated images were generated as described in (Clark et al., 2013), using custom scripts written in MATLAB. The simulation starts with two dimensional data, corresponding to a simple spherical cell shape of 3 μm diameter, drawn with a 5 nm resolution. The simulated cell has a cell membrane thickness of 15 nm and a cell wall thickness of 200 nm. To best represent the experimental imaging conditions, the cell membrane was assumed to be uniformly stained, and only 5 nm of the most outer part of the cell wall was uniformly stained in another color. To account for the experimental noise and finite background signals inside and outside of the cell, two different Gaussian noises were added. The mean and standard deviation of the noise was determined so that the noise in the final image matches typical experimental signals. The original image was then convoluted with a Gaussian function with a standard deviation of 200 nm corresponding to the point spread function. The smoothed data were sampled at 40 nm to generate the final pixelized image. To systematically test for the effects of finite signals in the cytoplasm, we kept the standard deviation of the noise and changed only its mean values. The generated images were analyzed using the same scripts as for the experimental data described above.

The simulation results suggest that the inside-outside difference in the background signal could potentially influence cell wall thickness measurement (Figure S1D). By running a systematic modification of background difference between inside and outside, and signal/noise ratio in simulations, we thus computed the influence of those parameters on the error in thickness measurement (Figure S1E). Those results defined a region in which the predicted error is below 30 nm, which is less than 20 % of the typical experimental thickness. We thus used this simulation result as a criterion for image quality, and discarded images or regions of images where the predicted error is out of this accepted region (Figure S1E). For CLEM analysis, however, we systematically observed a much higher intracellular background due to chemical fixation. In that context we thus implemented a correction script to extract the true signal peak by using an analytical expression of the convoluted intensity profile (Clark et al., 2013).

TEM and CLEM Images

The full cell wall in electron microscopy images was detected using custom scripts written in MATLAB, by using a threshold value for the signal intensity. In some images with inhomogeneous contrast, the results were manually updated. The edge of the binarized signal were traced to define the inside and outside boundaries of the cell wall. The normal direction was defined based on the inside cell wall boundary, and the cell wall thickness was defined as the distance between inside and outside boundaries along the normal direction. To compare EM and light microscopy images in CLEM analyses (Figure 1B first panel and S2E-G), we defined four morphologically distinguishable points (two tips and two scars), and used these points to overlay the two images by matching the distance between them. Comparison on larger regions, was done by measuring thickness in EM pictures manually within 2 μm regions at 8 individual positions, and compared with an average value computed from light-microscopy measurement in the Matlab script (Figure 1B third panel).

Cell Shape, Growth and Polarity Factor Concentration Measurements

Cell length was generally measured using lectin signals in ImageJ. To compute old end elongation rates visible birth scars were used as fiducial reference landmarks. Tip curvature was computed from the lectin contour defined for cell wall measurements, by fitting a local circle in Matlab (Bonazzi et al., 2015).

To analyze changes in cell shape, growth rates and localization of polar factors following turgor reduction by sorbitol addition, we developed dedicated Matlab scripts. We first segmented cells using the signal from the lectin-labelled cell wall. To this aim, we first smoothed the image with median and Gaussian filters and detected cell edges using the Laplacian of the Gaussian filter. The resultant binary image was then filtered to remove small segments. Given that the signal of the labelled cell wall has a finite thickness, we detected the inner and the outer border of this signal. All spaces in this image are then filled in white except for the spaces between the inner and outer border of the wall, yielding a black band representing the cell wall. Using the watershed algorithm, we finally

extracted the whole-cell contour defined as the middle of this band. To compute cell length, we fitted the long axis of the segmented cell with a polynomial of degree 3. This fit was then used to define a ''cell spine'' and its length was calculated, and used as a measure for cell length.

The whole-cell contour could then be manipulated using morphological and logical operations to obtain a set of arbitrary regions (tips, cytoplasm, etc.). The tip regions are for instance shaped as a cut off from the whole-cell mask perpendicular to the cell spine at specific distances along the spine. A segment outside of the cell can be shaped to compute the background.

Fluorescent signals of interest are then extracted from fluorescent images by using a mask based on corresponding sub-regions. The signal from the tips is corrected for the background signal and for bleaching. This is done by normalizing the background corrected tip signal with the background corrected cytoplasm signal:

$$I_{tip} = \frac{I_{tip\ raw} - I_{bg}}{I_{cytoplasm} - I_{bg}}$$

Strain-Stress Assay Simulation

The estimation procedure of cell mechanical parameters was similar to the one described in the paragraph ''Measurement of material properties'' in (Abenza et al., 2015) with the exception that, here, the cell wall thickness is measured all around the cell contour. For each cell, we followed steps described here:

1. Symmetrization of both the plasmolyzed contour and the turgid contour of each cell; the same symmetrization was kept for the thickness profile.
2. The plasmolyzed contour was swelled at different pressure steps (pressure is normalized by the Young modulus at the equator) assuming a distribution of thickness, and mechanical parameters away from the equator. Two different distributions of thickness were tested: (i) averaged plasmolyzed thickness and (ii) measured plasmolyzed thickness. Three distributions of Young modulus were tested: (i) a zero-parameter (i.e. constant Young modulus) and (ii and iii) two two-parameters distributions ("cos" and "sigmoid"), with one parameter describing the tip width and the other parameter accounting for the ratio between the Young modulus at the tip and the equator. As two recent articles (Abenza et al., 2015; Atilgan et al., 2015) consistently reported a zero-value for the in-plane Poisson ratio, this ratio was set to 0.01 for all the simulations.
3. Among the pressure steps and tested parameters, the ones for which the swelled plasmolyzed contour best fitted the turgid contour were retained to estimate mechanical parameters. Independently of the distribution of Young moduli, the selected normalized pressure step provided a ratio between the Young modulus at the equator and the internal turgor. The turgor pressure inside fission yeast cells has been estimated to be 1.5 MPa in (Atilgan et al., 2015) providing an absolute estimate of the Young moduli.

Variation in local Young moduli were simulated using:

a) A "sigmoid" distribution on the form: $Y(s)=Y_{tip}+(Y_{side}-Y_{tip})(sigmf(s,[5\ d])-sigmf(s,[5\ arc-d]))$, with s, the curvilinear coordinate, d the width along cell tip, and arc the total arclength. The "sigmoid" distribution (sigmf in Matlab) is flat at the equator, decreases sharply at a distance d from the tips, then is flat again at the tips.

Deviation from the computationally swollen cell and the original cell before turgor reduction was calculated as a distance from the best-fit. For tip sizes of 2.5 μm; 3 μm and 3.5 μm we obtained respective values for Y_{side}/P of 48.1±0.7; 49.0±0.8 and 48.9±0.8 ; for Y_{tip}/Y_{side} of 0.59±0.02; 0.63±0.02 and 0.68±0.02 with distances to best fits of 0.048±0.001; 0.050±0.001; 0.053±0.001.

Those values suggested that the lowest distance from the best fit are obtained for a small enough tip-width d. The value of E_{cyl}/P were not very sensitive to d whereas E_{tip}/E_{cyl} increased with d. The correlation between E_{tip} and E_{cyl} was not significant for d below 3 (p-value>0.5 for both the Pearson and Spearman tests) whereas it became significant for d=3.5 μm (p-value 0.02 Pearson, 0.11 Spearman).

b) A "cos" distribution: $Y(s)=Y_{tip}+(Y_{cyl}-Y_{tip})(0.5(1-\cos(2\pi s/arc)))^{d}$. The "cos" distribution is narrower around the equator than the sigmoid one especially for d>1 μm. Similarly to the sigmoid distribution, the best fit were obtained when the Young modulus decreased in the slowest manner from the equator (d=0.5, d=1). The estimations of Y_{cyl}/P were very sensitive to d as the decrease from the equator became very sharp when d=2. They were also higher than with the "sigmoid" fit in order to compensate for the quicker decrease at the equator. For the best fit (d=0.5, d=1), the estimated ratio of Y_{tip}/Y_{side} are slightly lower than for "sigmoid" ones. Obtained values are for exponent d of 0.5, 1 and 2 respectively: Y_{side}/P : 48.6±0.5, 54.9±0.5 and 73.6±0; Y_{tip}/Y_{cyl}: 0.46±0.02, 0.49±0.07 and 0.39 with distances from best-fit of 0.045; 0.048 and 0.065.

Spectrum Analysis of Thickness Fluctuations

Fourier-transform analyses were performed on two independent data sets on signals from time-lapses at 6' intervals, using custom-made Matlab scripts. The first data set consisted of 60' long videos of n=25 individual cells taken at random position in the cell cycle (Figure S4F). The second data set consisted of 210' long videos of n=8 individual cells taken from the beginning to the end of one cell

cycle (Figure S4G). For the first data set, we subtracted the mean thickness for each cell, and computed the amplitude of the discrete Fourier transform on the frequency domain. In the second data set we performed a short-time Fourier transform analysis, by subtracting for each cell trace a smoothed signal generated with a rectangular window. The spectrum was robust to changes in window width from 7 up to 17 time-points (42' to 102'). Both analyses yielded peaks corresponding to a full period of 50 to 60 min, supporting the consistency of this analysis.

Analytical Models for Tip Thickness Fluctuations

Equation 4 of the main text can be written in the form:

$$\frac{dh_{tip}}{dt}(t) = -a + b\frac{1}{h_{tip}(t-T)}, \qquad \text{(Equation S1)}$$

with $a = \frac{rPR_c}{Y} - S_0$, and $b = \lambda\frac{rPR_c}{Y}$.

Using T as a unit of time and the homeostatic thickness value b/a as a unit of thickness, this equation can be rewritten as:

$$\frac{d\bar{h}_{tip}}{d\bar{t}}(\bar{t}) = A\left(-1 + \frac{1}{\bar{h}_{tip}(\bar{t}-1)}\right) \qquad \text{(Equation S2)}$$

with $\bar{h}_{tip} = \frac{a}{b}h_{tip}$, $\bar{t} = t/T$, and $A = a^2T/b$. Numerical solutions of this ordinary differential equation were obtained using the NDSolve function of Mathematica (Wolfram Research Inc.). Equation S2 has damped solutions with no oscillations for $A < A_1$, oscillating damped solutions for $A < A < A_2$, and sustained oscillations for $A > A_2$. The values of A_1 and A_2 increase when $\bar{h}_{tip}(0)$ departs from 1. Analytical calculations show that when $\bar{h}_{tip}(0)$ is close to 1, $A_1 = exp(1)$ and $A_2 = \pi/2$. Optimal homeostasis corresponds to maximal damping, which occurs for, $A = A_1$. Coming back to initial model parameters, $A = \left(S_0 - \frac{rPR}{Y}\right)^2 T \Big/ \left(\lambda\frac{rPR}{Y}\right)$. Therefore, a decrease in λ yields an increase in A, and hence to fluctuations with higher amplitude.

3D Cell Growth Model

The growth model developed in (Abenza et al., 2015) was modified to include varying thickness and varying young modulus. The parameters h (thickness) and Y (Young modulus) (Formula 36-38 in the supplemental material of (Abenza et al., 2015)) are no more constant.

The thickness distribution profile has been selected by the following procedure: all the symmetrized thickness profiles were linearly re-parametrized from new end to old end so that the new end lays at curvilinear abscissa 0 and the old end at a curvilinear abscissa of 13.9. After this operation all the thickness profiles were averaged, the average was very well fitted by a three-parameters linear combination of sigmoids. The three parameters h_{ne}, h_{oe} and h_{side} are the cell wall thickness at the new end, at the old end, and at the equator.

Only the modification to the original algorithm are detailed here (Supplemental material of Abenza-Martinez *et al* (Abenza et al., 2015)):

- At step *n* (iii), once the new curvilinear abscissa s_n has been calculated using formula 46, arc_n, the total arclength is updated and the thickness profile can also be updated using the shape family

$$h_n(s_n) = h_{ne} + \frac{h_{side} - h_{ne}}{1 + e^{-2.20(s_n - 2.36)}} - \frac{h_{side} - h_{oe}}{1 + e^{-73.3(s_n - arc_n + 2.36)/arc_n}} \qquad \text{(Equation S3)}$$

as well as the Young modulus distribution:

$$Y_n(s_n) = 62 + \frac{38}{1 + e^{-2.20(s_n - 2.36)}} - \frac{30}{1 + e^{-73.3(s_n - arc_n + 2.36)/arc_n}} \qquad \text{(Equation S4)}$$

- The amplitude of each step of growth in formula (47-48) is: $\delta = 1.2$
- The model for the fluorescence profile K of the polarity marker is:

$$K(s) = 1.037\exp\left(-0.4165\left|\frac{s}{D}\right|^{1.745}\right) \qquad \text{(Equation S5)}$$

where D=1.17, 1.06 and 0.93 depending on which strain is modeled *rga4Δ*, wt and *rga2Δ*. Each of the D constants have been chosen such that the asymptotic radius of convergence of the cell corresponds to a value close to the experimental tip radii 1.76 μm (*rga4Δ*), 1.62 μm (wt) and 1.46 μm (*rga2Δ*). The cell wall tip thicknesses of *rga4Δ*, wt and *rga2Δ* are 0.149 μm, 0.166 μm and 0.179 μm.

DATA AND SOFTWARE AVAILABILITY

The software for live cell wall thickness measurement is available at: http://www.minclab.fr/research/.

All the other image analysis scripts developed in the context of this study can be made available upon request.